

Do tidally-generated inertial waves heat the subsurface oceans of Europa and Enceladus?

Rovira-Navarro, Marc; Rieutord, Michel; Gerkema, Theo; Maas, Leo R.M.; van der Wal, Wouter; Vermeersen, Bert

DOI

[10.1016/j.icarus.2018.11.010](https://doi.org/10.1016/j.icarus.2018.11.010)

Publication date

2019

Document Version

Accepted author manuscript

Published in

Icarus

Citation (APA)

Rovira-Navarro, M., Rieutord, M., Gerkema, T., Maas, L. R. M., van der Wal, W., & Vermeersen, B. (2019). Do tidally-generated inertial waves heat the subsurface oceans of Europa and Enceladus? *Icarus*, 321, 126-140. <https://doi.org/10.1016/j.icarus.2018.11.010>

Important note

To cite this publication, please use the final published version (if applicable). Please check the document version above.

Copyright

Other than for strictly personal use, it is not permitted to download, forward or distribute the text or part of it, without the consent of the author(s) and/or copyright holder(s), unless the work is under an open content license such as Creative Commons.

Takedown policy

Please contact us and provide details if you believe this document breaches copyrights. We will remove access to the work immediately and investigate your claim.

Accepted Manuscript

Do tidally-generated inertial waves heat the subsurface oceans of Europa and Enceladus?

Marc Rovira-Navarro, Michel Rieutord, Theo Gerkema,
Leo R.M. Maas, Wouter van der Wal, Bert Vermeersen

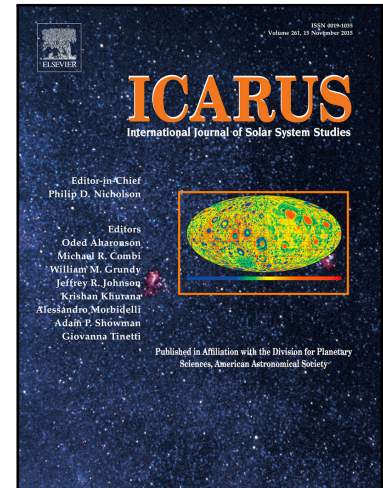
PII: S0019-1035(18)30471-8
DOI: <https://doi.org/10.1016/j.icarus.2018.11.010>
Reference: YICAR 13092

To appear in: *Icarus*

Received date: 16 July 2018
Revised date: 6 November 2018
Accepted date: 12 November 2018

Please cite this article as: Marc Rovira-Navarro, Michel Rieutord, Theo Gerkema, Leo R.M. Maas, Wouter van der Wal, Bert Vermeersen, Do tidally-generated inertial waves heat the subsurface oceans of Europa and Enceladus?, *Icarus* (2018), doi: <https://doi.org/10.1016/j.icarus.2018.11.010>

This is a PDF file of an unedited manuscript that has been accepted for publication. As a service to our customers we are providing this early version of the manuscript. The manuscript will undergo copyediting, typesetting, and review of the resulting proof before it is published in its final form. Please note that during the production process errors may be discovered which could affect the content, and all legal disclaimers that apply to the journal pertain.



Highlights

- Tidal forces induce internal inertial waves in Europa's and Enceladus' oceans.
- Internal waves focus energy along internal shear layers that propagate in the ocean.
- Inertial waves can focus tidal dissipation at the poles.
- Inertial waves can result in ocean currents of significant amplitude (a few cm/s).
- For an ocean of constant thickness, inertial waves cannot prevent freezing.

ACCEPTED MANUSCRIPT

Do tidally-generated inertial waves heat the subsurface oceans of Europa and Enceladus?

Marc Rovira-Navarro^{a,b,*}, Michel Rieutord^{c,d}, Theo Gerkema^e, Leo R.M. Maas^{f,a}, Wouter van der Wal^b, Bert Vermeersen^{b,e}

^a*NIOZ Royal Netherlands Institute for Sea Research, Department of Ocean Systems OCS, and Utrecht University, P.O. Box 59, 1790 AB Den Burg, Texel, the Netherlands*

^b*TU Delft, Faculty of Aerospace Engineering (AE), Building 62 Kluyverweg 1, P.O. Box 5058, 2629 HS Delft / 2600 GB Delft, The Netherlands*

^c*Université de Toulouse, UPS-OMP, IRAP, Toulouse, France*

^d*CNRS, IRAP, 14, avenue Edouard Belin, 31400 Toulouse, France*

^e*NIOZ Royal Netherlands Institute for Sea Research, Department of Estuarine and Delta Systems EDS, and Utrecht University, P.O. Box 140, 4400 AC Yerseke, the Netherlands*

^f*Faculty of Science, Department of Physics, Institute for Marine and Atmospheric Research Utrecht, Utrecht University P.O. Box 80.005, 3508 TA Utrecht*

Abstract

Some of the moons of the outer solar system harbour subsurface liquid oceans. Tidal dissipation plays an important role in preventing these oceans from freezing. In the past, most studies considered only tidal dissipation in the solid layers of these bodies (rock and ice). Recently, new studies considering tidal dissipation in the oceans of these moons have appeared. All of them make use of the shallow water approximation. However, the use of this approximation might not be adequate. Here we consider the linear non-hydrostatic three dimensional response of these oceans to tidal forcing with the full Coriolis force. To do so we consider an ocean of homogeneous density contained within a perfectly spherical shell and neglect the effect of the ice shell. We force the ocean with a time changing tidal potential and observe patterns of periodic inertial waves that take energy from the global tidal forcing and focus it along thin shear layers that propagate in the fluid. We focus on Europa and Enceladus, showing that inertial waves result in fluid flows of significant amplitude (a few cm/s). Nevertheless, we find that under the previously mentioned assumptions tidal dissipation due to inertial waves is several orders of magnitude smaller than Europa's radiogenic heating and Enceladus' observed heat flux. Finally, we propose additional dissipation mechanisms that might play a relevant role in Europa and Enceladus and could be further investigated.

Keywords: Tides, Enceladus, Europa, Rotational dynamics

*Corresponding author

Email address: marc.rovira@nioz.nl (Marc Rovira-Navarro)

1. Introduction

Evidence for underground water reservoirs in some of the moons of the outer solar system has accumulated over the last few decades. The existence of a subsurface water body in Europa was first hypothesised by Cassen et al. (1979). They argued that radiogenic and tidal heating could melt Europa's interior and form an ocean. The hypothesis was confirmed when Khurana et al. (1998) and Kivelson et al. (2000) reported variations of the magnetic field in Europa associated with an induced magnetic field and showed that a layer of subsurface salty water is consistent with these observations. The existence of a subsurface ocean is also consistent with the complex geology of Europa's surface (e.g., Pappalardo et al., 1999).

The case of Enceladus is markedly different. This tiny moon of Saturn, its radius being just over 250 km, features vigorous geological activity. Cassini flybys revealed water plumes emanating from long parallel cracks (nicknamed tiger-stripes) on the South Pole (Porco et al., 2006; Spencer et al., 2006). The detection of salt-rich grains in the plumes (Postberg et al., 2009, 2011) and evidence of hydrothermal activity within the moon (Hsu et al., 2015) indicate that the plumes originate from an underground water reservoir. The observed forced libration of Enceladus' surface reveals that the ocean is not only restricted to the moon's southern pole but it completely decouples the ice shell from the moon's rocky mantle (Thomas et al., 2016).

Far away from the Sun, these oceans cannot be maintained by solar irradiation. Another heat source is therefore needed to prevent them from freezing; this heat source is most likely tidal dissipation. Due to orbital resonances with Io and Ganymede, Europa orbits Jupiter in an eccentric orbit. Similarly, in the Saturnian system, Enceladus' eccentricity is maintained by an orbital resonance with Dione. The orbital eccentricity results in a time-varying tidal potential that raises a prominent tide. The moons' obliquity results in additional latitudinal librations of the tidal bulge. Most studies focused on studying tidal dissipation in the solid layers of Europa and Enceladus (e.g., Ojakangas and Stevenson, 1989; Roberts and Nimmo, 2008). These studies show that the European ocean can be maintained by tidal and radiogenic heating; thermal models suggest that the ocean might be around 100 km thick (Hussmann et al., 2002). This is, however, not the case of Enceladus, where tidal and radiogenic heating in the solid parts of the moon are not sufficient to prevent a global ocean from freezing (Tobie et al., 2008; Bêhoukova et al., 2017) unless Enceladus has an unconsolidated rocky core (Choblet et al., 2017).

By analogy with Earth, where most tidal energy dissipation occurs in the ocean, it has been suggested that tidal dissipation within the ocean plays a major role. Tyler (2008) was the first to propose that oceanic tidal currents could heat the moons of the outer solar system. Tyler (2008) considered the response of an ice-free shallow ocean of constant density. He solved the Laplace Tidal Equations (LTE) using the method of Longuet-Higgins (1968) for the different tidal constituents. He showed that Europa's obliquity excites planetary Rossby waves of considerable amplitude and suggested that this mechanism might close Enceladus' thermal energy budget (Tyler, 2009). However, it was later found that the obliquity of Enceladus is too small for this mechanism to generate enough tidal heating (Chen and Nimmo, 2011). Tyler (2014) and Hay and Matsuyama (2017) also showed that

43 the eccentricity tide can generate sufficient tidal heating but only for unrealistically shallow
44 oceans. Subsequent studies considered the effect that the ice shell has on oceanic tidal
45 dissipation and concluded that the ice crust further dampens the ocean response (Beuthe,
46 2016; Matsuyama et al., 2018).

47 A possible criticism to the previous studies is the assumption of an ocean of constant
48 density. An unstratified ocean filters out internal gravity waves which have an important role
49 in tidal dissipation and mixing in Earth's ocean (Garrett, 2003). There is little information
50 about the stratification of Europa's and Enceladus' oceans. The ocean is heated from the
51 bottom by tidal and radiogenic heat within the silicate mantle, likely creating a well-mixed
52 convecting ocean (Goodman et al., 2004; Goodman and Lenferink, 2012; Soderlund et al.,
53 2013). Nevertheless, under certain conditions the ocean might be stratified (Melosh et al.,
54 2004; Vance and Brown, 2005). We do not challenge the assumption of an unstratified ocean
55 and focus on the other assumptions underlying the LTE.

56 The main assumption of the LTE is that the ocean is in hydrostatic equilibrium, cur-
57 rents are predominantly horizontal. Because vertical currents are assumed to be small, the
58 hydrostatic approximation is often used together with the traditional approximation, which
59 consists in neglecting the terms of the Coriolis force linked to vertical motions in the ocean
60 (Gerkema et al., 2008). For an unstratified ocean these assumptions hold as long as the ratio
61 of the characteristic vertical and horizontal length scales is small (see Vallis (2006)). Using
62 the ocean thickness and body's radius as a measure of vertical and horizontal length scales,
63 respectively, higher ratios are obtained for Europa and Enceladus than for Earth (~ 0.06
64 and ~ 0.15 versus ~ 0.001). It is therefore expected that the neglected vertical velocity is
65 of more relevance in these bodies, making the LTE incomplete to describe tidal currents in
66 Europa's and Enceladus' subsurface oceans.

67 Without the hydrostatic and traditional approximations, new kinds of waves are possible
68 in the unstratified oceans of the icy moons, the so-called internal inertial (gyroscopic) waves
69 (Stern, 1963; Bretherton, 1964; Greenspan., 1969; Stewartson, 1971; Maas, 2001). These
70 waves have properties that are markedly different from those of the more familiar surface
71 waves (Maas, 2005) and have been suggested to be of importance for tidal dissipation in
72 giant planets and binary stars (Rieutord and Valdetaro, 1997; Rieutord et al., 2001; Ogilvie
73 and Lin, 2004; Rieutord and Valdetaro, 2010; Lainey et al., 2017). In this study, we want to
74 take the young field of "planetary oceanography" one step further by exploring the relevance
75 of inertial waves for tidal dissipation in the icy moons.

76 We consider an ocean contained within a deformable spherical shell and study tidally
77 induced inertial waves for different ocean thicknesses. Our main goal is to quantify the
78 amount of tidal heating that is generated by these waves to assess whether they are a sig-
79 nificant component in the thermal energy budget of these moons. Additionally, we compare
80 the flow amplitude of inertial waves to that of surface gravity waves obtained with the LTE
81 and consider the footprint that they might have on the satellites' surface. To do so we solve
82 the linearised incompressible Navier-Stokes equations for the different components of the
83 eccentricity and obliquity tide using the spectral methods developed to study inertial waves
84 in an astrophysical context (stars and giant planets) (e.g., Rieutord and Valdetaro, 1997;
85 Ogilvie and Lin, 2004; Rieutord and Valdetaro, 2010).

86 The text is structured as follows: Section 2 introduces inertial waves and presents their
 87 main properties, in Section 3 we give the mathematical formulation of the problem, we
 88 introduce the tidal potential and then explain how the linearised Navier-Stokes equations
 89 are forced with this tidal forcing. Afterwards, the results are shown and discussed (Section
 90 4) and conclusions are presented (Section 5)

91 2. Properties of Internal Inertial Waves

92 To understand the properties of internal inertial waves we start by considering a simplified
 93 situation. We consider an inviscid fluid of constant density (ρ_0) inside a container rotating
 94 with angular velocity Ω . For this situation, the mass and momentum conservation equations,
 95 written in a co-rotating frame, are given by (e.g., Le Bars et al., 2015):

$$96 \quad \nabla \cdot \mathbf{u} = 0, \quad (1a)$$

$$97 \quad \frac{\partial \mathbf{u}}{\partial t} + \mathbf{u} \cdot \nabla \mathbf{u} + 2\Omega \times \mathbf{u} = -\nabla W. \quad (1b)$$

98 \mathbf{u} is the fluid's velocity, W is a reduced pressure that contains the fluid pressure, the
 99 body's gravity potential and other possible conservative body forces. We neglect non-linear
 100 terms and seek plane wave solutions of the form:

$$101 \quad \mathbf{u} = \text{Re} [\tilde{\mathbf{u}} e^{i(\mathbf{k} \cdot \mathbf{x} + \omega t)}], \quad (2)$$

102 with \mathbf{k} the wavevector, $\tilde{\mathbf{u}}$ the wave amplitude and ω the wave frequency. Introducing this
 trial solution to Equation (1) we obtain a dispersion relation of the form:

$$103 \quad \omega^2 = 4\Omega^2 \left(\frac{k_z^2}{k_x^2 + k_y^2 + k_z^2} \right), \quad (3)$$

104 where z is parallel to the rotational axis and x, y normal to it. This dispersion relation is
 105 markedly different from that of the more familiar surface-gravity waves. While for surface
 106 waves the frequency of the wave only depends on the magnitude of the wavenumber, for
 107 internal inertial waves it only depends on the angle that the wavevector forms with the
 108 rotational axis. The group velocity, ($\mathbf{c}_g = \frac{\partial \omega}{\partial \mathbf{k}}$) is perpendicular to the wavevector \mathbf{k} . Energy
 propagates along surfaces of constant slope which form an angle θ with the rotational axis:

$$109 \quad \theta = \arcsin \left(\frac{\omega}{2\Omega} \right), \quad (4)$$

the so-called characteristics (see Figure 1a).

110 These properties lead to a fundamental difference in how inertial waves behave upon
 111 reflection as compared to surface waves (e.g., Maas, 2005). When a monochromatic surface
 112 wave packet encounters a surface it reflects specularly without changing its wavelength.
 113 In contrast, an internal inertial wave packet reflects keeping the wavevector inclination
 114 with respect to the rotational axis constant. Upon reflection, the wavelength can change.

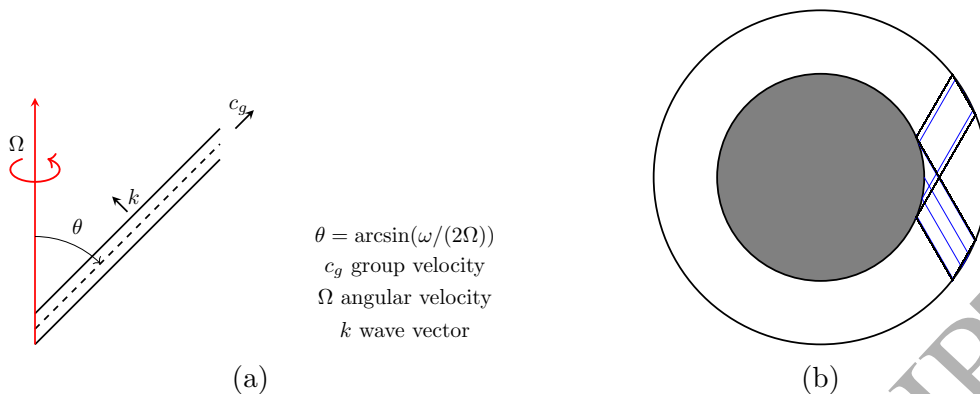


Figure 1: Inertial wave propagation. The wave packet propagates with group velocity \mathbf{c}_g following characteristics that form an angle θ with the rotational axis. The wavevector \mathbf{k} is perpendicular to the group velocity (a). (b) Depending on the container's geometry a wave packet (blue) can converge towards a periodic trajectory (black).

115 Depending on the container's geometry this can lead to focusing of the wave packet which
 116 becomes an efficient mechanism to transport energy from large to small scales.

117 The focusing properties of inertial waves can result in wave attractors. As its name
 118 indicates, wave attractors are trajectories in which energy accumulates. For ocean geome-
 119 tries that have focusing trajectories, two wave packets originating at different locations will
 120 converge towards the same trajectory (Figure 1b). Wave attractors have the peculiarity of
 121 focusing the energy of a large-scale forcing to smaller scales regardless of the nature and
 122 location of the excitation. This phenomenon has been observed in the laboratory, both for
 123 internal gravity waves (e.g., Maas et al., 1997; Brouzet et al., 2016) and internal inertial
 124 waves (e.g., Maas, 2001; Manders and Maas, 2003, 2004).

125 As it is of special relevance for astrophysical and geophysical applications, the propaga-
 126 tion of inertial waves in spherical containers has been widely studied (e.g., Bryan, 1889; Stern,
 127 1963; Bretherton, 1964; Greenspan., 1969; Stewartson, 1971, 1972; Rieutord and Valdettaro,
 128 1997; Ogilvie, 2009). The response of an inviscid fluid inside an spherical container is given
 129 by well-behaved eigenmodes (Bryan, 1889). However when a nucleus is added, wave at-
 130 tractors can develop which lead to singularities; velocity increases without bound along the
 131 attractor (Stewartson, 1971). Something similar happens at the critical latitude (Θ_c), the
 132 latitude at which a characteristic is tangent to the nucleus, where the velocity also develops
 133 a singularity (Rieutord et al., 2001). In reality, viscosity prevents the development of such
 134 singularities. The result is the development of prominent internal shear layers that propa-
 135 gate in the fluid domain following the characteristics where a significant amount of energy
 136 can be dissipated.

137 3. Problem Formulation

138 3.1. The tidal potential

139 The obvious candidate for the generation of inertial waves in the oceans of the icy moons is
 140 the tidal potential caused by the obliquity and eccentricity of the moons. We can express the

141 tidal potential in terms of the orbital elements of the satellite (Jara-Oru e and Vermeersen,
142 2011):

$$\Psi = (\omega R)^2 \left(\frac{r}{R} \right)^2 \{ \psi_0 + \psi_{ns} + \psi_{e0} + \psi_{e2} + \psi_{o1} \}, \quad (5)$$

143 where ω is the mean motion of the satellite given by $\omega^2 = GM_p/a^3$, G is the universal
144 gravitational constant, M_p the mass of the planet and a the semi-major axis of the satellite's
145 orbit. As we are considering tidally locked satellites, ω is the same as the rotational frequency
146 of the satellite (Ω). R is the satellite's radius and r the distance from the center of the
147 satellite to the considered point inside the satellite. The different components of the tidal
148 potential are (Jara-Oru e and Vermeersen, 2011):

$$\psi_0 = -\frac{1}{2}P_{2,0}(\cos \theta) + \frac{1}{4}P_{2,2}(\cos \theta) \cos(2\phi), \quad (6a)$$

$$\psi_{ns} = -\frac{1}{2}P_{2,2}(\cos \theta) \sin(2\phi + \Omega_{ns}t) \sin(\Omega_{ns}t), \quad (6b)$$

$$\psi_{e0} = -\frac{3e}{2}P_{2,0}(\cos \theta) \cos(\omega t), \quad (6c)$$

$$\psi_{e2} = \frac{e}{4}P_{2,2}(\cos \theta) [3 \cos(2\phi) \cos(\omega t) + 4 \sin(2\phi) \sin(\omega t)], \quad (6d)$$

$$\psi_{o1} = P_{2,1}(\cos \theta) \sin(\epsilon) \cos(\phi) \sin(\Phi + \omega t). \quad (6e)$$

149 θ and ϕ are the co-latitude and longitude in the body-fixed reference frame, respectively. ψ_0
150 is the static component of the tidal potential, ψ_{ns} arises due to non-synchronous rotation.
151 The eccentricity tide is given by ψ_{e0} , which is caused by the variation in distance between
152 the planet and the satellite; and ψ_{e2} , caused by the east/west libration of the position of
153 the subplanet point on the moon's surface. On the other hand, the obliquity tide, ψ_{o1} , is
154 the result of the latitudinal libration of the subplanet point due to the satellite's obliquity.
155 $P_{l,m}$ are the associated Legendre polynomials of degree l and order m and Φ , e and ϵ are the
156 argument of pericenter, the eccentricity and the obliquity of the moon, respectively. We only
157 consider degree two terms of the tidal potential, as the amplitude of the other components
158 rapidly decreases with increasing degree as $(r/a)^l$.

159 The non-axisymmetric term of the eccentricity tide (ψ_{e2}) and the obliquity tide (ψ_{o1})
160 can be further divided in a westward (ψ_{e2w} , ψ_{o1w}) and an eastward (ψ_{e2e} , ψ_{o1e}) propagating
161 wave:

$$\psi_{e2} = \psi_{e2e} + \psi_{e2w} = \frac{7e}{8}P_{2,2}(\cos \theta) \cos(2\phi - \omega t) - \frac{e}{8}P_{2,2}(\cos \theta) \cos(2\phi + \omega t), \quad (7)$$

$$\psi_{o1} = \psi_{o1e} + \psi_{o1w} = \frac{\sin(\epsilon)}{2}P_{2,1}(\cos \theta) \sin(\phi - \omega t - \Phi) - \frac{\sin(\epsilon)}{2}P_{2,1}(\cos \theta) \sin(\phi + \omega t + \Phi). \quad (8)$$

Table 1: Physical parameters for Europa and Enceladus. Radius (R), mass (M), average density (ρ_{av}), surface gravity (g) and rotational rate (Ω) are obtained from: <https://ssd.jpl.nasa.gov/?horizons> and Chen et al. (2014). The obliquity (ϵ) of Europa and Enceladus are obtained assuming that the moons are in a Cassini state (Baland et al., 2012; Chen and Nimmo, 2011). The maximum amplitude of the different components of the equilibrium tide are computed considering a non-self gravitating ice-free ocean surrounding an infinitely rigid core (Equation (17)) and using the maximum value of the satellites' obliquity. The argument of pericenter (Φ) and ocean density (ρ_o) are assumed to be 0 and 1000 kg m^{-3} , respectively.

	Europa	Enceladus
R [km]	1565.0	252.3
M [kg]	$4.797 \cdot 10^{22}$	$1.0805 \cdot 10^{20}$
ρ_{av} [kg m^{-3}]	2990	1606
g [m s^{-2}]	1.31	0.11
Ω [rad s^{-1}]	$2.05 \cdot 10^{-5}$	$5.31 \cdot 10^{-5}$
e [-]	0.0094	0.0047
ϵ [deg]	< 0.1	< 0.0015
$z_{e0}^{(eq)}$ [m]	11.08	11.50
$z_{e2e}^{(eq)}$ [m]	19.39	20.13
$z_{e2w}^{(eq)}$ [m]	2.77	2.88
$z_{o2e}^{(eq)}$ [m]	1.03	0.003
$z_{o2w}^{(eq)}$ [m]	1.03	0.003
Φ [deg]	0	0
ρ_o [kg m^{-3}]	1000	1000

162 For this study we consider the different components of the eccentricity and obliquity tide
 163 and ignore the non-synchronous rotation of the satellite. We also ignore the static component
 164 of the tidal potential as it does not induce a dynamic ocean response. The relevant physical
 165 parameters of Europa and Enceladus are given in Table 1.

166 3.2. Governing equations and assumptions

167 In contrast to Section 2, we now consider the fluid to be viscous and expand the reduced
 168 pressure in its different components. The equations of motion can be written as:

$$169 \quad \nabla \cdot \mathbf{u} = 0, \quad (9a)$$

$$\frac{\partial \mathbf{u}}{\partial t} + \mathbf{u} \cdot \nabla \mathbf{u} + 2\boldsymbol{\Omega} \times \mathbf{u} = -\frac{1}{\rho_0} \nabla p' + \frac{1}{\rho_0} \nabla \cdot \boldsymbol{\tau} - \nabla \Psi - \nabla \Psi'. \quad (9b)$$

170 The primed quantities denote deviations from hydrostatic equilibrium. Ψ' represents the
 171 gravitational potential of the body, p' is the fluid pressure and $\boldsymbol{\tau}$ the stress tensor of the
 172 fluid, which we assume to follow Stokes' constitutive law:

$$\boldsymbol{\tau} = \mu(\nabla \mathbf{u} + \nabla \mathbf{u}^T), \quad (10)$$

173 where μ is the dynamic molecular viscosity. We further use perturbation theory and consider
 174 the different quantities to be small. Under such consideration the non-linear advective term

175 $(\mathbf{u} \cdot \nabla \mathbf{u})$ is neglected. The validity of this assumption will be discussed later (Section 5). We
 176 introduce an effective viscosity μ_{eff} which is higher than the molecular viscosity of the fluid
 177 and accounts for non-modelled small-scale dissipation mechanisms (e.g., turbulent mixing,
 178 interactions of waves with turbulent convection, etc.).

179 Finally, we obtain the non-dimensional form of the equations of motion by using the
 180 inverse of the satellite's rotational frequency $(2\Omega)^{-1}$ and the satellite radius (R) as time and
 181 length scales respectively:

$$\hat{\nabla} \cdot \hat{\mathbf{u}} = 0, \quad (11a)$$

$$\frac{\partial \hat{\mathbf{u}}}{\partial \hat{t}} + \mathbf{e}_z \times \hat{\mathbf{u}} = -\hat{\nabla} \hat{W} + E \hat{\nabla}^2 \hat{\mathbf{u}}, \quad (11b)$$

183 with \mathbf{e}_z the direction of the satellite's rotational axis, W again the reduced pressure:

$$W = \frac{p'}{\rho_o} + \Psi + \Psi' \quad (12)$$

185 and the non-dimensional variables (indicated with a hat) and parameters defined as:

$$\mathbf{u} = 2\Omega R \hat{\mathbf{u}}, \quad (13a)$$

$$W = 4\Omega^2 R^2 \hat{W}, \quad (13b)$$

$$E = \frac{\mu_{eff}}{2\rho\Omega R^2}, \quad (14a)$$

$$\hat{\omega} = \frac{\omega}{2\Omega}. \quad (14b)$$

186 We have introduced the non-dimensional Ekman number (E), which gives the ratio of viscous
 187 to Coriolis forces; and the non-dimensional frequency ($\hat{\omega}$), which, since the problem is forced
 188 at the diurnal tidal frequency, equals 0.5. In the discussion that follows we use the non-
 189 dimensional equations; to avoid cumbersome notation we drop the hat from the variables.

191 As a starting point we assume that the moons have a free surface. If the surface wave
 192 speed (\sqrt{gh} , with g the satellite's surface gravity and h the ocean depth) is high enough
 193 so that the ocean adjusts quickly to forces varying at the tidal potential frequency, we can
 194 assume that the radial displacement of the ocean surface is given by the equilibrium tide
 195 (Tyler, 2008; Ogilvie, 2009). This assumption breaks down if the ocean is too shallow, in
 196 that case surface gravity waves dominate the ocean response and other kinds of resonances
 197 occur (Matsuyama et al., 2018). For the icy moons, the surface wave speed is high enough as
 198 long as the oceans are thicker than 0.78 km or 1.6 km for Europa and Enceladus, respectively.
 199 With ocean thicknesses of ~ 100 km (Hussmann et al., 2002) and ~ 38 km (Beuthe et al.,
 200 2016) for Europa and Enceladus respectively, the previous assumption seems reasonable for
 201 the problem at hand.

202 We follow the approach of Ogilvie (2005) and Rieutord and Valdetaro (2010) and split
 203 the fluid response into two components: the equilibrium tide $\mathbf{u}^{(eq)}$ plus a dynamical tide $\mathbf{u}^{(d)}$.
 204 By using this decomposition Equation (11) becomes:

$$\frac{\partial \mathbf{u}^{(d)}}{\partial t} + \mathbf{e}_z \times \mathbf{u}^{(d)} = -\nabla W + E \nabla^2 \mathbf{u}^{(d)} + \mathbf{f}^{(eq)}. \quad (15)$$

205 $\mathbf{f}^{(eq)}$ is an inertial force associated with the equilibrium tide given by:

$$\mathbf{f}^{(eq)} = -\frac{\partial \mathbf{u}^{(eq)}}{\partial t} - \mathbf{e}_z \times \mathbf{u}^{(eq)}. \quad (16)$$

206 Note that the dynamic tide is forced indirectly through the equilibrium tide as it does not
 207 satisfy the momentum equation (Ogilvie and Lin, 2004). If we consider a non self-gravitating
 208 ocean around an infinitely rigid core with a free-surface the equilibrium tide is simply given
 209 by:

$$\mathbf{z}_{l,m}^{(eq)} = \frac{\Psi_{l,m}}{g} \mathbf{e}_r, \quad (17)$$

210 where $\Psi_{l,m}$ is the degree l order m component of the tidal potential. The maximum ampli-
 211 tude of the equilibrium tide for Europa and Enceladus for the different tidal components is
 212 given in Table 1. If the effect of self-gravitation, the finite rigidity of the core or the presence
 213 of an ice-shell is considered the equilibrium tide can be obtained as:

$$\mathbf{z}_{l,m}^{(eq)} = Z_{l,m} \frac{\Psi_{l,m}}{g} \mathbf{e}_r, \quad (18)$$

214 with $Z_{l,m}$ being an admittance factor. Matsuyama et al. (2018) showed that an ice shell
 215 dampens the response of the ocean resulting in $Z_{l,m}$ to be smaller than or close to 1. In
 216 particular, for realistic ice shell thicknesses, the admittance is close to 1 for Europa while it
 217 can be more than one order of magnitude smaller for Enceladus. In this work, we assume the
 218 ocean to follow the equilibrium tide of an ice-free, non self-gravitating ocean in a satellite
 219 with a infinitely rigid core (Equation (17)). By doing so, we obtain an upper bound of tidal
 220 dissipation due to inertial waves in a spherical shell shaped ocean.

221 We assume the system to have a response with the same frequency as the forcing tidal
 222 potential and thus we consider the different fields to be proportional to $e^{i\omega t}$. By doing so we
 223 can eliminate time from the equations of motion and we are left with the system:

$$\nabla \cdot \mathbf{u}^{(d)} = 0, \quad (19a)$$

$$i\omega \mathbf{u}^{(d)} + \mathbf{e}_z \times \mathbf{u}^{(d)} = -\nabla W + E \nabla^2 \mathbf{u}^{(d)} + \mathbf{f}^{(eq)}, \quad (19b)$$

$$\mathbf{f}^{(eq)} = -i\omega \mathbf{u}^{(eq)} - \mathbf{e}_z \times \mathbf{u}^{(eq)}. \quad (19c)$$

226 We solve Equations (19) in a spherical shell, assuming no-slip boundary conditions at
 227 the fluid-solid interfaces ($\mathbf{u}_d = 0$).
 228

229 3.3. Numerical Approach

230 We solve Equations (19) for the different constituents of the equilibrium tide (Equation
 231 (17)). As we did with the tidal potential, we expand the equilibrium tide into its different
 232 constituents: the order 0 eccentricity tide ($\mathbf{u}_{e0}^{(eq)}$), and the eastward and westward components
 233 of the order 2 eccentricity tide and order 1 obliquity tide ($\mathbf{u}_{e2e}^{(eq)}$, $\mathbf{u}_{e2w}^{(eq)}$ and $\mathbf{u}_{o1e}^{(eq)}$, $\mathbf{u}_{o1w}^{(eq)}$) (see
 234 Appendix A). We then solve Equations (19) using $\omega = 0.5$ and $\omega = -0.5$ for the westward
 235 and eastward propagating components respectively.

236 We use the method of Rieutord and Valdettaro (1997, 2010), which is detailed in Ap-
 237 pendix A. We make use of the spherical symmetry of the problem and expand the velocity
 238 and reduced pressure fields using L spherical harmonics in the horizontal direction. The
 239 resulting equations are discretised in the radial direction using Chebyshev polynomials on
 240 $N + 1$ Gauss-Lobatto collocation nodes. By doing so, Equation (19) and the boundary con-
 241 ditions result in an algebraic system of $(L - m + 1)(N + 1)$ linear equations. The associated
 242 matrix of this linear system is block-tridiagonal, and the system is solved using classical LU-
 243 factorization of a banded matrix. Except where otherwise indicated, the resolution, given
 244 by L and N , is chosen so that the truncation error is less than $\sim 10^{-4}$.

245 We are specially interested in computing tidal dissipation due to the tidally-induced
 246 flows. We compute the amplitude of tidal dissipation as (e.g., Ogilvie and Lin, 2004):

$$\hat{D}_v = 2E \int_V \mathbf{c}_{ij}^* \mathbf{c}_{ij} dV, \quad (20)$$

247 where c_{ij} are the elements of the rate-of-strain tensor, $c_{ij} = \frac{1}{2}(\partial_i u_j + \partial_j u_i)$. We expand
 248 Equation (20) using spherical harmonics as indicated in Appendix B.

249 4. Results

250 4.1. Parameter Regime

251 The two parameters that control the fluid response are the ocean thickness and the Ekman
 252 number. We characterise the thickness of the ocean using the ratio of the inner to outer ocean
 253 radius, η . Europa's and Enceladus' ocean thicknesses are still not known. To understand
 254 the effect of ocean geometry on the propagation of inertial waves, we explore the range $\eta =$
 255 $0.3 - 0.99$, which corresponds to ocean thicknesses ranging from 1095.5 to 15.7 km for Europa
 256 and 176.6 to 2.5 km for Enceladus. For this range we use a resolution of $\Delta\eta = 0.005$ which
 257 is equivalent to ocean thickness changes of 7825 m for Europa and 1262 m for Enceladus.
 258 However, current estimates suggest an η of ~ 0.93 (Hussmann et al., 2002) for Europa and
 259 ~ 0.85 (Beuthe et al., 2016) for Enceladus. It is for this reason that we further explore the
 260 range $\eta = 0.8 - 0.99$ using a $\Delta\eta$ of 0.0005.

261 The Ekman number depends on the fluid viscosity (Equation (14)). If we compute
 262 the Ekman number using the molecular viscosity of water we obtain a value of 10^{-14} and
 263 10^{-13} for Europa and Enceladus respectively. These low Ekman numbers require currently
 264 unattainable resolutions. In any case, when linearising the equations of motion we have
 265 introduced a new effective dynamic viscosity (μ_{eff}) that accounts for small-scale dissipation

266 mechanisms. Given our limited knowledge about these oceans it is difficult to estimate the
 267 appropriate value of this parameter. It is however expected that the effective viscosity will
 268 be orders of magnitudes higher than the molecular viscosity (e.g., Ogilvie and Lin, 2004). In
 269 the following experiments we explore a wide range of Ekman numbers ($E = 10^{-4} - 10^{-10}$)
 270 to account for this uncertainty.

271 We first study the propagation of inertial waves for different ocean thicknesses and Ekman
 272 numbers and explain the main characteristics in terms of the properties defined in Section
 273 2 such as wave attractors and the critical latitude singularity (Section 4.2). Afterwards,
 274 we focus on tidal dissipation and quantify the relevance of inertial waves for Europa's and
 275 Enceladus' thermal energy budget (Section 4.3)

276 4.2. Wave attractors and the critical latitude singularity

277 As explained in Section 2 the response of the fluid is dominated by the convergence of wave
 278 packets towards wave attractors and the critical latitude singularity. We start by studying
 279 the structure of wave attractors that are excited by tidal forcing. As the moons are phase-
 280 locked, the frequency of the forcing equals the rotational frequency of the moon, hence, the
 281 angle that the characteristics form with the vertical is 30° (Figure 1a). We use ray-tracing to
 282 study the propagation of energy in meridional planes of the fluid domain. The intersection
 283 of the characteristic surfaces with a meridional plane are straight lines (rays) along which
 284 energy propagates. We launch a wave packet from a point on the inner sphere without zonal
 285 velocity and follow its propagation along the characteristics until it converges towards an
 286 attractor in the same meridional plane. Note that when a wave packet is launched with a
 287 zonal component it may end up trapped in a meridional plane or escape meridional trapping
 288 and reflect endlessly around the domain (Rabitti and Maas, 2013, 2014). However, because
 289 of the symmetry of the tidal potential with respect to rotation around the z axis we focus
 290 on wave attractors in the meridional plane.

291 We launch a wave ray from a point equatorward of the critical latitude (5°) and one
 292 poleward (85°). The latitude of the last 100 inner boundary reflections are then noted and
 293 shown in a Poincaré plot in Figure 2a. Additionally, we compute the Lyapunov exponent,
 294 which measures the asymptotic rate at which two neighbouring rays converge:

$$\Lambda = \lim_{N \rightarrow \infty} \sum_{n=1}^N \log \left| \frac{d\Theta_{n+1}}{d\Theta_n} \right|. \quad (21)$$

295 $d\Theta$ is the angular distance between the reflection points of two neighbouring characteristics.
 296 High (in absolute value) Lyapunov exponents mean highly attracting wave attractors while a
 297 Lyapunov exponent equal to 0 indicates non-attracting trajectories. The Lyapunov exponent
 298 for different ocean geometries is displayed in Figure 2b.

299 We distinguish between two types of attractors: equatorial attractors, trapped equator-
 300 ward of the critical latitude, and polar attractors, with reflections outside the previously
 301 mentioned interval. As can be seen in Figure 2a, the shape of the attractor depends on the
 302 ratio of inner to outer ocean radius (η). For some ocean geometries, attractors with few
 303 reflections (short attractors) and high (in absolute value) Lyapunov exponents exist. This is

304 the case of the band $[0.5775, 0.6545]$ and $[0.7235, 0.7420]$. In the first case, both equatorial
 305 and polar attractors exist, while for the second only polar attractors appear. The peak for
 306 $\eta = 0.6545$ corresponds to an attractor with reflections infinitesimally close to the critical
 307 latitude, where there is nearly infinite focusing. For such attractors, the Lyapunov exponent
 308 goes to minus infinity as resolution in η increases (Rieutord et al., 2001).

309 For $\eta < 0.57$, there are non-attracting periodic trajectories with a Lyapunov exponent
 310 close to 0. In fact, it can be shown that for $\eta \leq 0.5$ all trajectories associated with the fre-
 311 quency $\omega/2\Omega = 0.5$ are strictly periodic and have a Lyapunov exponent equal to 0 (Rieutord
 312 et al., 2001). For these ocean geometries if a ray is launched from the inner sphere it will
 313 eventually return to the same point after some reflections, explaining the horizontal lines in
 314 Figure 2a.

315 The response of the fluid is characterised by the opposing effects of wave focusing and
 316 viscous diffusion. The focusing effect of the geometry tends to focus energy towards small
 317 scales ultimately leading to a singularity along the wave attractor. On the other hand,
 318 viscosity diffuses the velocity countering the geometrical focusing effect and the development
 319 of wave attractors. As we will now see, these two competing effects determine whether a
 320 wave attractor is excited for a particular ocean geometry or not.

321 We start by choosing two ocean geometries with a high (in absolute value) Lyapunov
 322 exponent, $\eta = 0.63$ and $\eta = 0.73$, and force the fluid with the axisymmetric eccentricity
 323 tidal component for two different Ekman numbers, 10^{-7} and 10^{-9} . To achieve a truncation
 324 error less than $\sim 10^{-4}$, we use a resolution of $L = 500$ and $N = 200$ for $E = 10^{-7}$ and
 325 $N = 200$ and $L = 1200$ for $E = 10^{-9}$. A meridional cut of the sphere showing the amplitude
 326 of the kinetic energy and viscous dissipation is shown in Figure 3. For this tidal component
 327 the plots are independent of the meridional cut. Also superimposed, we show the wave
 328 attractors characteristic of these two ocean geometries.

329 As can be seen, in both cases wave attractors are generated. Internal shear layers are
 330 clearly observed along the attractors where both kinetic energy and viscous dissipation are
 331 enhanced. As in Rieutord and Valdettaro (2010) we observe the importance of the critical
 332 latitude singularity for producing the attractor. The attractor seems to be “fed” by the
 333 shear layer emanating from for critical latitude. As expected, as the Ekman decreases the
 334 internal shear layer becomes thinner.

335 We also explore the behaviour of the fluid for ocean geometries with a low (in absolute
 336 value) Lyapunov exponent. In such cases, the critical latitude singularity dominates the flow
 337 (Ogilvie and Lin, 2004; Ogilvie, 2009; Rieutord and Valdettaro, 2010). We distinguish two
 338 cases: ocean geometries where periodic non-focusing trajectories exist (e.g., $\eta = 0.35, 0.5$),
 339 $\Lambda = 0$, and geometries with long weakly-attracting wave attractors (e.g., $\eta = 0.75, 0.8815$),
 340 $\Lambda < 0$. For the first case, the shear layer emitted from the critical latitude propagates
 341 following the characteristics and widens slowly due to viscous dissipation and the lack of
 342 focusing (Figures 4a-4b). In contrast, for the second case we observe the focusing of the
 343 shear layer upon reflection (Figures 4c-4e).

344 For $\eta = 0.75$ and 0.8815 we observe that as the ray approaches the polar regions both
 345 kinetic energy and dissipation are enhanced (Rieutord and Valdettaro, 1997). The effect of
 346 changing the Ekman number is similar to that reported for those cases where wave attractors

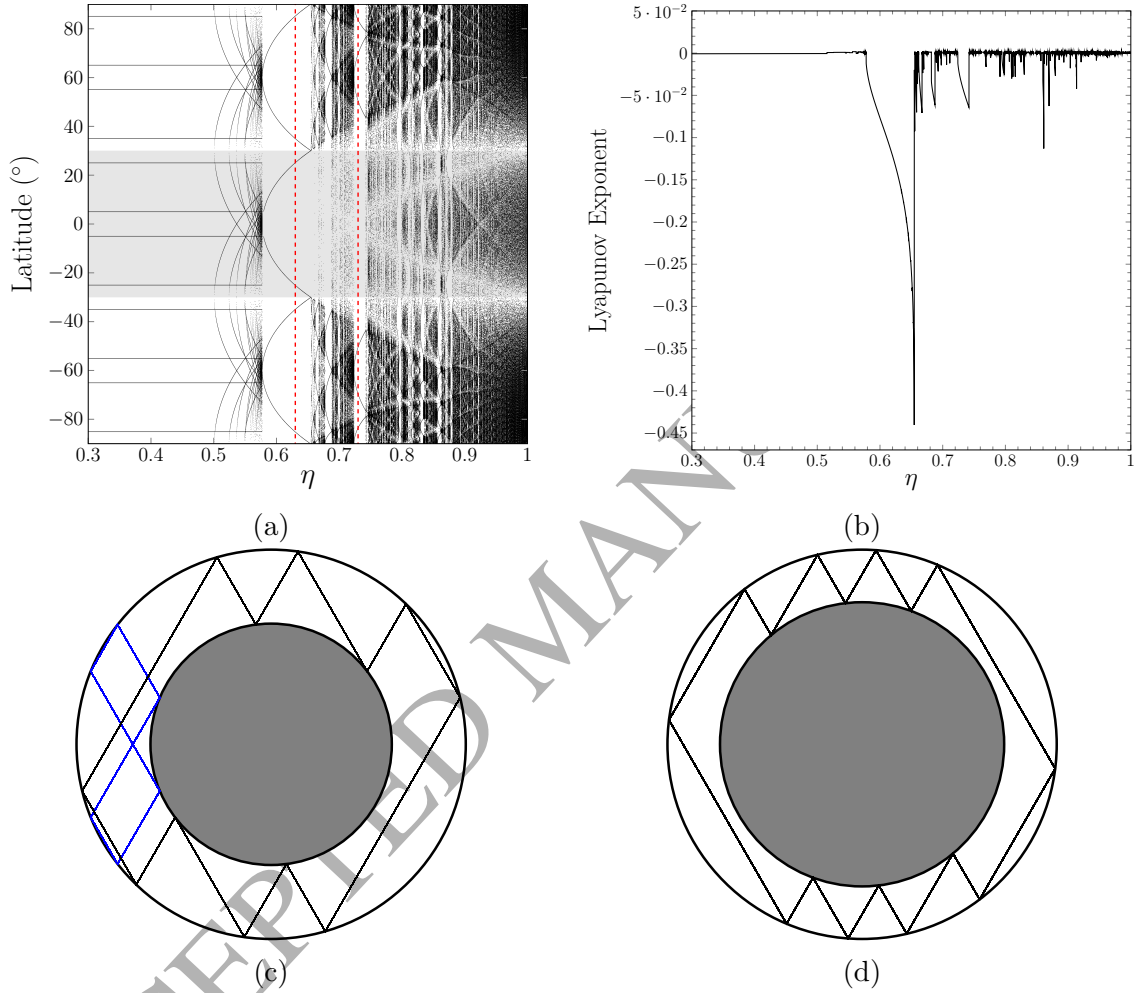


Figure 2: Poincaré plot (a) and Lyapunov exponent (b) for a forcing frequency of $\omega/(2\Omega) = 0.5$. In (a) the latitude of the last 100 reflection points on the inner sphere for rays launched from $\pm 5^\circ$ and $\pm 85^\circ$ latitude are indicated for different inner to outer ocean radius ratios (η). The shaded region indicates reflections equatorward of the critical latitude. Two specific ocean geometries for which short, highly attracting wave attractors exist ($\eta = 0.63, 0.73$) are indicated in red and shown in (c) and (d), respectively. (b) gives the Lyapunov exponent for the polar attractors.

347 appear. It is expected that if the Ekman number is sufficiently small the focusing effect will
 348 prevail over viscous diffusion leading to the generation of long wave attractors for $\eta = 0.75$
 349 and 0.8815 similar to those observed for $\eta = 0.63$ and 0.73 . However, the low Ekman number
 350 for which this transition occurs requires resolutions currently computationally unattainable.

351 The case of $\eta = 0.8815$ is especially interesting as it corresponds to an Enceladan ocean
 352 thickness of around 30 km, which is close to current estimates for Enceladus (Thomas et al.,
 353 2016; Čadek et al., 2016; Beuthe et al., 2016). For this ocean thickness we compute the
 354 maximum velocity amplitude of inertial tides and study the possible manifestation of inertial
 355 waves on Enceladus' surface. We find that the maximum velocity amplitude varies from 0.5
 356 to 3 cm/s for Ekman numbers ranging from 10^{-7} to 10^{-10} . Moreover, the maximum velocity
 357 amplitude is always encountered in polar regions. These currents are stronger than those
 358 induced by the eccentricity tide under the shallow water approximation, which for realistic
 359 ocean thicknesses have a magnitude of around 1 mm/s (Tyler, 2009).

360 Vermeersen et al. (2013) suggested that wave attractors in a polar ocean basin could
 361 be the origin of Enceladus' tiger-stripes; here we investigate this hypothesis for the present
 362 configuration (an unstratified global ocean of constant depth). Interaction between the fluid
 363 and the ice shell are likely to occur at the inertial waves reflection points, where we observe
 364 enhanced dissipation. For a 30 km thick ocean, we observe that the pressure at these points
 365 is in the order of ~ 1 Pa. Moreover, we can estimate the melting rate of the ice shell at
 366 these points by assuming that all the energy dissipated in a ray is focused there and does
 367 not radiate outwards. We obtain a maximum melting rate in the order of 1 m every 10
 368 kyr. Even though it is unclear how inertial waves would interact with the ice shell, these
 369 numbers suggest that in an ocean of constant thickness it is unlikely that tidally-excited
 370 inertial waves could be the origin of observed surface features, such as the tiger stripes.
 371 More work is needed to study if other ocean geometries can result in enhanced energy
 372 focusing and higher stresses.

373 *4.3. Tidal dissipation*

374 The main focus of this work is to study tidal dissipation within Europa and Enceladus. We
 375 start by assuming an Ekman number of 10^{-7} and compute tidal dissipation for the different
 376 tidal constituents and different ocean thickness ($\eta = 0.3 - 1$) as detailed in Appendix B
 377 (Section 4.3.1). To strengthen our conclusions we analyse the effect of varying the Ekman
 378 number on the degree-two order-zero tidal constituent (Section 4.3.2). For the different
 379 shell geometries we first vary the Ekman number between $10^{-4} - 10^{-8}$. We then study the
 380 asymptotic behaviour of dissipation with decreasing Ekman number for some relevant shell
 381 geometries for which we use an Ekman number as low as 10^{-10} .

382 *4.3.1. Tidal dissipation for the different tidal components*

383 Dissipation due to tidally induced inertial waves in Europa and Enceladus for $E = 10^{-7}$,
 384 is shown in Figure 5. As a reference, we also indicate the estimated value of radiogenic
 385 heating in Europa (Hussmann et al., 2010) and the observed thermal output of Enceladus'
 386 tiger stripes (Spencer et al., 2013).

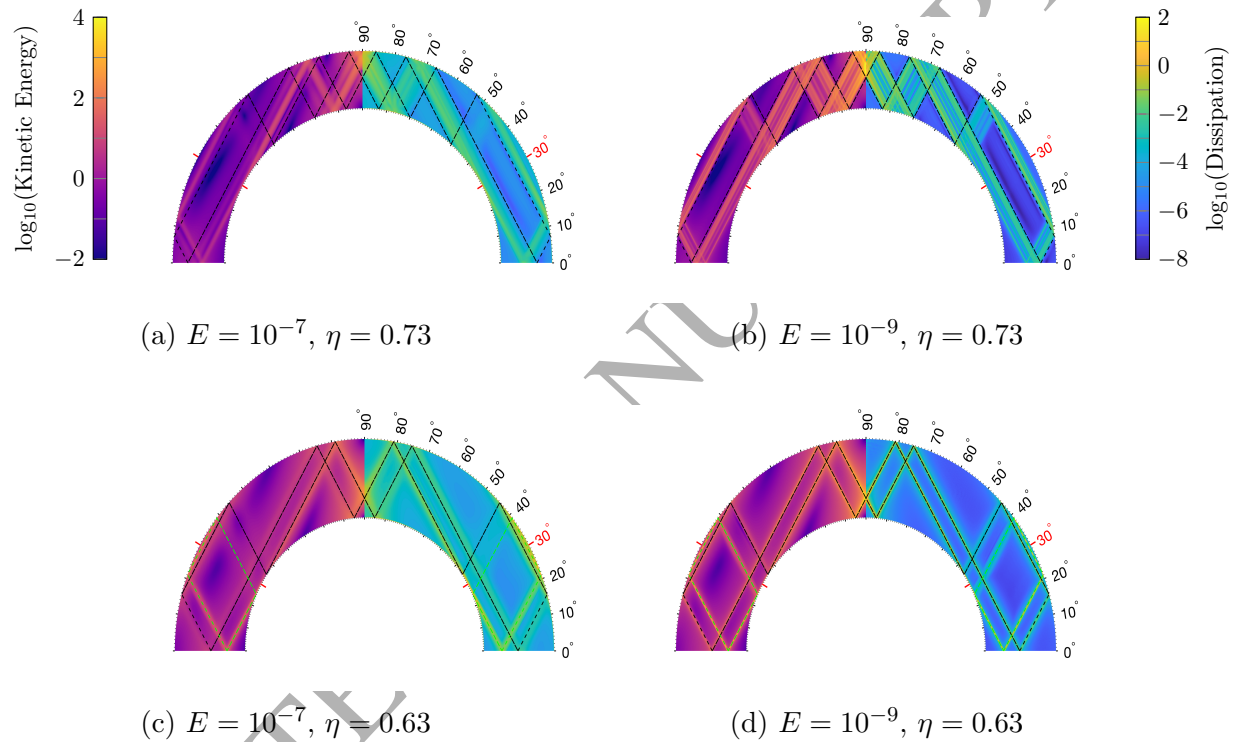


Figure 3: Non-dimensional kinetic energy (left quadrant) and viscous dissipation (right quadrant) amplitude due to the degree two, order zero eccentricity tide for two ocean geometries where short wave attractors exist. The patterns are shown for different Ekman number (E) and inner to outer ocean radius ratio (η). Polar and equatorial wave attractors are superimposed in black and green, respectively, and the critical latitude is indicated in red. A logarithmic scale is used both for kinetic energy and viscous dissipation. The maximum values of the non-dimensional colour-scale correspond to a kinetic energy of 0.65 J m^{-3} and 4.69 J m^{-3} ; and a viscous dissipation of $0.26 \text{ } \mu\text{W m}^{-3}$ and $4.97 \text{ } \mu\text{W m}^{-3}$ for Europa and Enceladus, respectively.

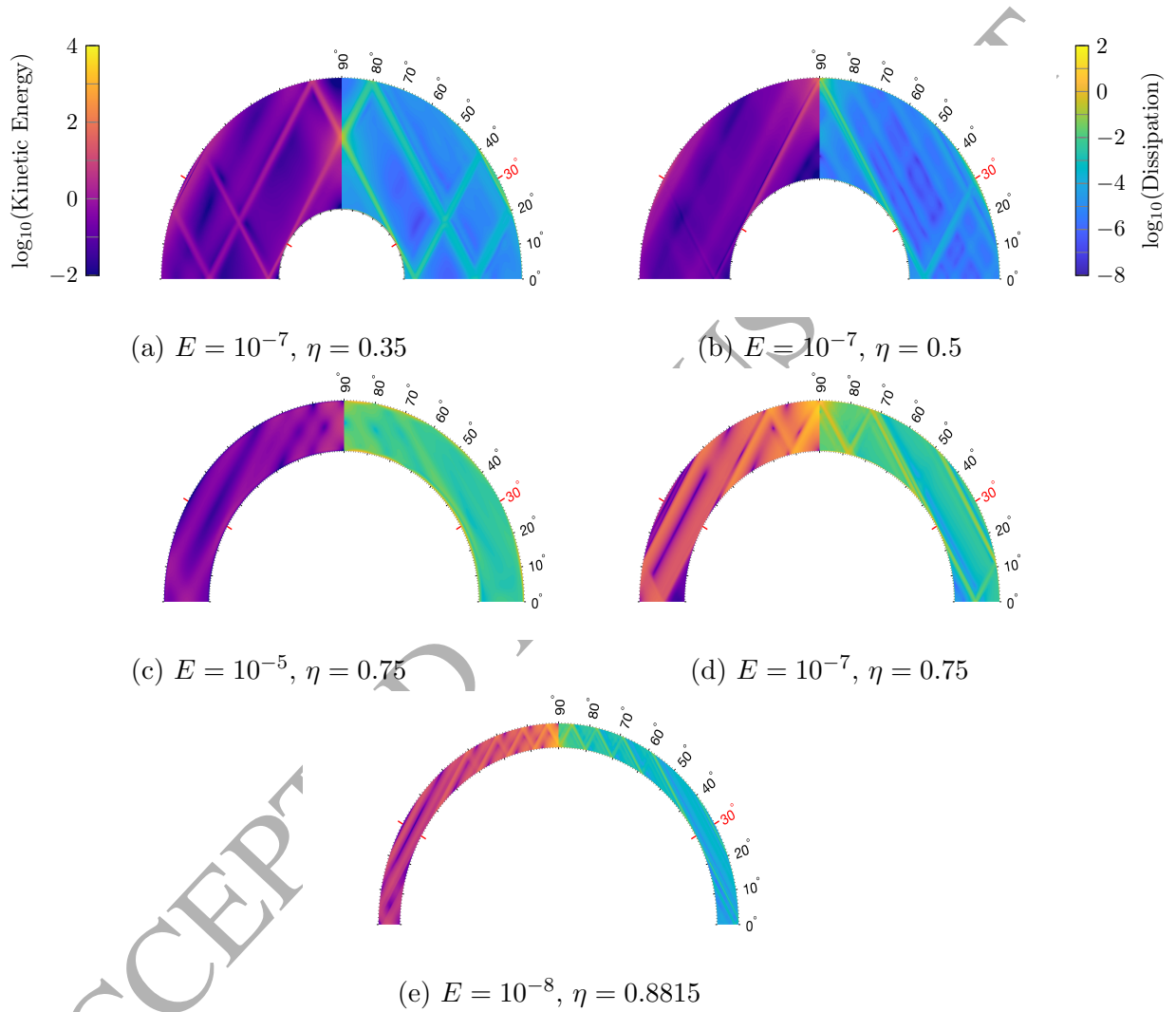


Figure 4: Same as Figure 3 but for ocean geometries with a small Lyapunov exponent. Rays emanating from the critical latitude (and not wave attractors) dominate the flow response.

387 It can be seen that the values of the tidal dissipation are well below the reference values
 388 for both Europa and Enceladus. Moreover, when we consider the region of the plot that
 389 corresponds to likely values of ocean thickness on Europa and Enceladus, $\eta > 0.9$ (Anderson
 390 et al., 1998; Hussmann et al., 2002) and $\eta > 0.8$ (Thomas et al., 2016; Ćadek et al., 2016;
 391 Beuthe et al., 2016), respectively, we observe that the values of tidal dissipation are several
 392 orders of magnitude smaller than radiogenic heating in Europa and the observed heat flux
 393 in Enceladus. Nevertheless, it is interesting to study the contribution of the different tidal
 394 constituents. We see that the axisymmetric eccentricity and eastward tide dominate the
 395 fluid response. Moreover, the order one obliquity tide produces considerably lower tidal
 396 dissipation, especially in Enceladus. This fact follows from the small amplitude of this tidal
 397 component as compared with the others (see Table 1) .

398 For most tidal constituents the tidal dissipation curve is markedly spiky (Figure 5). There
 399 are values of η for which dissipation is enhanced by more than one order of magnitude. The
 400 complex system of internal-shear layers that arise due to the singularities of the problem
 401 results in different values of dissipation for different ocean geometries. This is not the case
 402 of the westward propagating obliquity tide whose dissipation is given by a much smoother
 403 curve. This is because for a degree two, order one forcing the equations of motion admit
 404 a purely toroidal solution (Rieutord and Valdetaro, 1997), the so called “spin-over” mode.
 405 This solution is an exact solution of the equations of motion in case stress-free boundary
 406 conditions are used.

407 However, when no-slip boundary conditions are used for the westward obliquity tide
 408 the “spin-over” mode disappears. The use of no-slip boundary conditions results in the
 409 development of an oscillatory Ekman layer at the solid-liquid boundary. The thickness of
 410 this Ekman layer scales with $\approx E^{1/2}$, however at the critical latitude it thickens and scales as
 411 $\sim E^{2/5}$ over a region of width $\sim E^{1/5}$ (Hollerbach and Kerswell, 1995; Kerswell, 1995). The
 412 thickening of the Ekman layer breaks the symmetry of the problem and launches inertial
 413 waves that propagates in the interior. However, the resulting internal shear layers are weaker
 414 in this case than those generated by the other tidal constituents, dissipation is dominated
 415 by the Ekman layer that forms in the solid-liquid boundary which is less dependent on the
 416 shell geometry.

417 4.3.2. *Dependence of tidal dissipation on Ekman number*

418 We study the dependence of tidal dissipation with Ekman number. For a given ocean
 419 thickness (η) we distinguish three different cases depending on the behaviour of viscous
 420 dissipation in the limit $E \rightarrow 0$. Dissipation can increase, decrease or become asymptotically
 421 constant. We call the first and second cases resonance and anti-resonance, respectively,
 422 after Rieutord and Valdetaro (2010). As we will see, the last case is associated with the
 423 appearance of a wave-attractor Note that this definition differs from the classic definition of
 424 a resonance, commonly associated with the excitation of eigenmodes.

425 We start by varying the Ekman number from 10^{-4} to 10^{-8} for the axisymmetric eccen-
 426 tricity tide (Figure 6). For low Ekman numbers ($E = 10^{-4}, 10^{-5}$) the flow is dominated by
 427 the Ekman boundary layer formed at the solid-fluid boundary and not internal shear layers
 428 and wave attractors (see Figure 4c). For such cases the dissipation curve is smooth, similarly

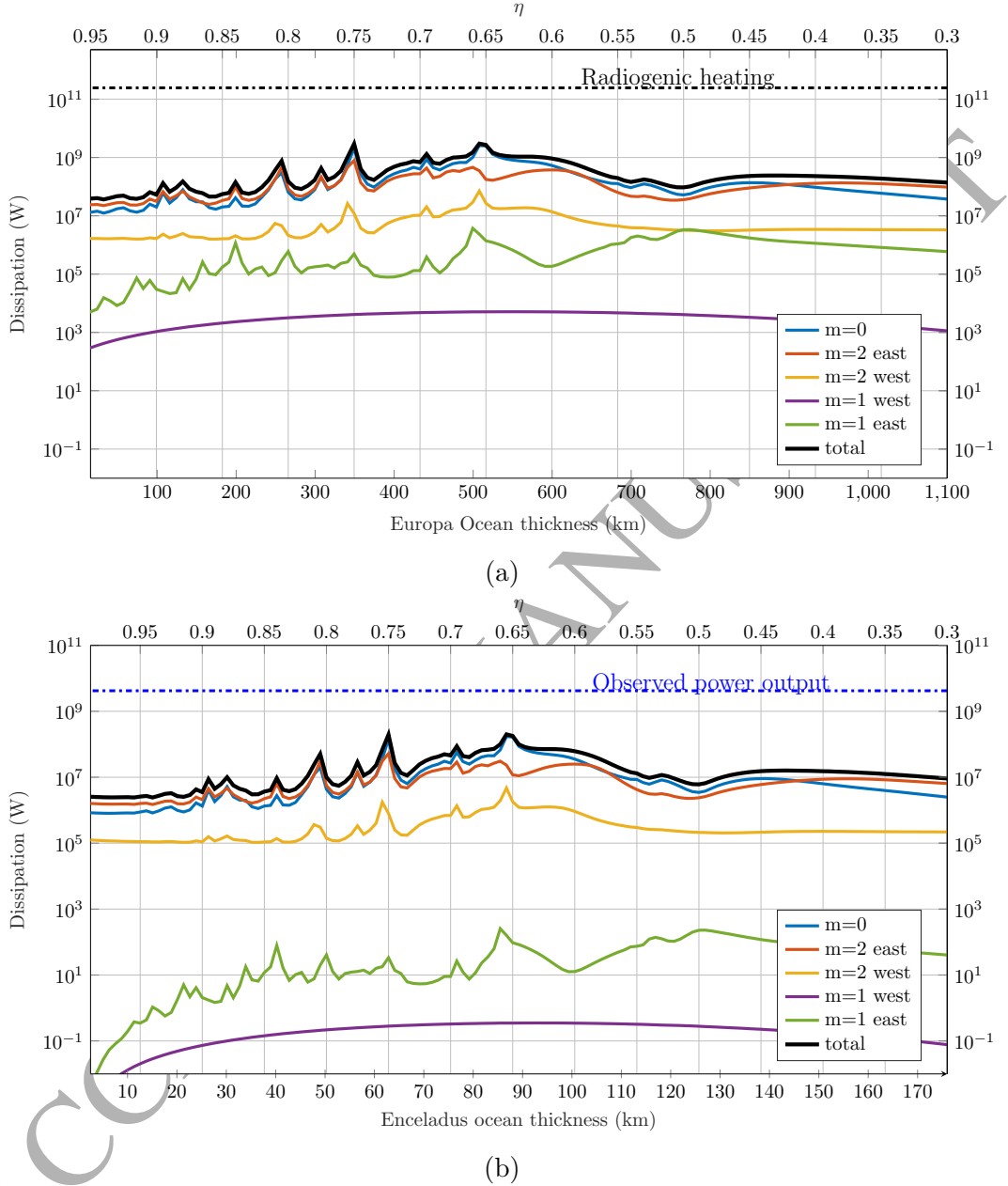


Figure 5: Tidal dissipation amplitude due to tidally excited inertial waves in Europa (a) and Enceladus (b). The ocean is assumed to be within a spherical shell of constant thickness (inner to outer ocean radius ratio, η). All values are computed using $E = 10^{-7}$. The axisymmetric and non-axisymmetric components of the eccentricity tide ($m = 0$ and $m = 2$) as well as the obliquity tide ($m = 1$) are considered. As reference, an estimate of Europa's radiogenic heating and the power radiated from Enceladus tiger stripes are indicated.

429 to the westward order one obliquity tide. As the Ekman number decreases, internal shear
 430 layers and wave attractors become the dominant features of the fluid response and the curve
 431 becomes more spiky.

432 We see that for small values of η dissipation decreases with Ekman number, an anti-
 433 resonance. The behaviour becomes more complicated for thinner oceans for which resonances
 434 occur for some values of η (e.g., 0.75, 0.807, 0.8415, 0.8815), moreover, we see that these cases
 435 correspond to local maxima of tidal dissipation (in η). We select some representative cases
 436 of η in which we observe wave attractors ($\eta = 0.63$ and 0.73), anti-resonances ($\eta = 0.35$)
 437 or resonances ($\eta = 0.76$ and 0.8815) for further study. For these cases we further explore
 438 the change of dissipation as the Ekman number decreases (Figure 7). We use an Ekman
 439 number as low as 10^{-10} , which requires enhanced resolution ($L = 2000$, $N = 350$) to achieve
 440 a truncation error of $\sim 10^{-3}$.

441 For a thick ocean ($\eta = 0.35$), dissipation decreases with decreasing Ekman number.
 442 Dissipation approximately follows a power law of the form $\sim E^{0.35}$. As explained, for this
 443 ocean geometry, strictly non-attracting periodic trajectories exist. Rieutord and Valdetaro
 444 (2018) have shown that in such a situation the fluid responds to the excitation with a
 445 flow characterised by an ever increasing wavenumber that ultimately, when $E=0$, inhibits
 446 any response. This is actually the anti-resonance associated with the periodic trajectory
 447 $\omega = \sin(\pi/6)$.

448 We now consider the two cases with highly attracting short wave attractors, $\eta = 0.63$
 449 and $\eta = 0.73$, depicted in Figure 3. Figure 7 shows that for these two cases dissipation
 450 tends towards an asymptotic limit. In a wave attractor there is a balance between focusing
 451 and diffusion. As the Ekman number is reduced, the thickness of the internal shear layer is
 452 reduced and the velocity gradient increased in such a way that dissipation remains constant.
 453 This situation is similar to that observed in Ogilvie (2005) who showed the asymptotic
 454 convergence of dissipation in wave attractors in a rectangular container. It is also interesting
 455 to note that the asymptotic limit is reached at higher Ekman numbers for $\eta = 0.63$ than for
 456 $\eta = 0.73$. Figure 3 shows that the $\eta = 0.73$ attractor is longer and less attracting, viscous
 457 dissipation acts along a longer distance and prevents the attractor from developing for high
 458 Ekman number.

459 Finally, we focus on two cases where a resonance occurs ($\eta = 0.75$ and 0.8815). These
 460 resonances are of special relevance if the Ekman number of Europa's and Enceladus' ocean is
 461 very low, for example close to that given by the molecular viscosity of water ($10^{-14} - 10^{-13}$).
 462 In such a case, if a resonant state is attained, dissipation could be considerably higher than
 463 the values computed for Ekman numbers several orders of magnitude higher. As seen in
 464 Figure 7, for these two cases dissipation increases with decreasing Ekman number until it
 465 reaches a maximum and then starts to decrease again. This behaviour can be understood
 466 by analysing the resonance peaks in Figure 6b. We see that as the Ekman number decreases
 467 the curve becomes more spiky, the resonance peak narrows. If the exact η for which the
 468 resonance occurs is not chosen, dissipation will decrease with decreasing Ekman number as
 469 the resonance peak becomes narrower. As is evident from this plot, our current resolution
 470 does not allow us to resolve the exact value of η at which dissipation reaches its maximum.

471 Higher resolution is needed in our explored parameter space to find the exact resonant

472 values of η . It is likely that at these exact resonant ocean geometries the actual dissipation for
 473 an Ekman number close to that given by the molecular viscosity of water ($E = 10^{-13} - 10^{-14}$)
 474 is several orders of magnitude higher than what we find in Figure 6. However, we need to
 475 recall that as the Ekman number decreases the resonance peak becomes narrower, thus a
 476 resonance would only occur over a very narrow range of ocean thicknesses. For instance, we
 477 see that by using $\Delta\eta = 126$ m for Enceladus or 783 m for Europa the resonance peak for
 478 $\eta = 0.8815$ at an Ekman number of 10^{-9} is already missed. It seems impossible that the ocean
 479 of Europa or Enceladus is of the thickness precisely required for such resonances to occur,
 480 specially since this would require the sea-floor and ice shell to be devoid of topographical
 481 features of higher amplitude than the previously mentioned resolution.

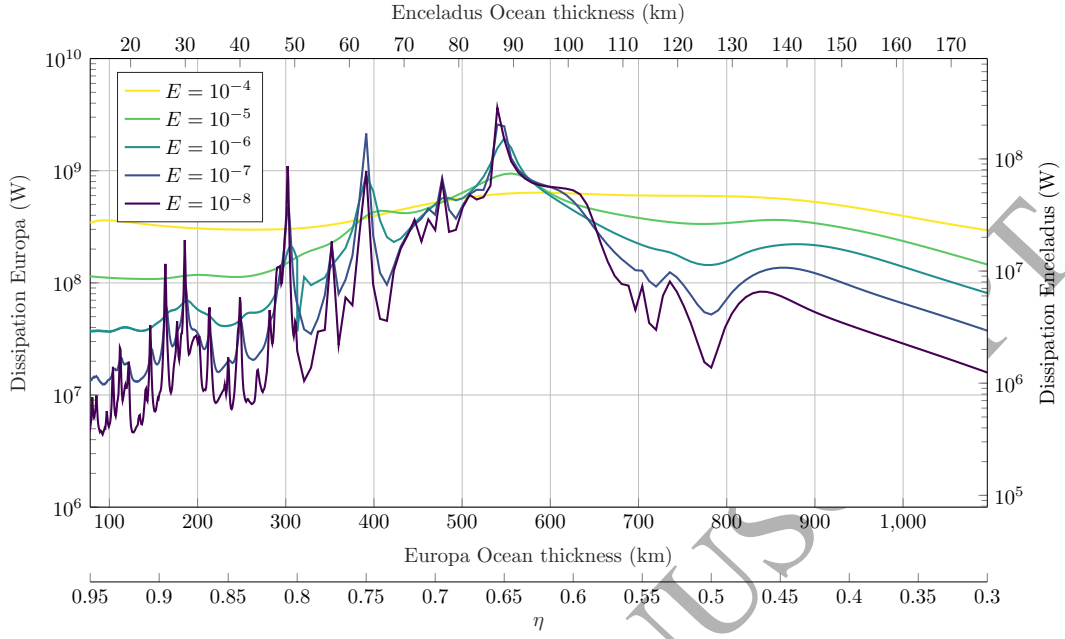
482 5. Discussion and Conclusions

483 In this work we analyse for the first time tidal dissipation due to inertial waves in Europa
 484 and Enceladus. We consider tides caused by the eccentric orbit of these satellites as well as
 485 their obliquity. We consider an ocean contained within a spherical shell and use a spectral
 486 method to compute tidal dissipation for different ocean thicknesses and dynamic viscosity
 487 coefficients (given by the Ekman number). We neglect the effect of the ice shell and argue
 488 that our results represent an upper bound estimate for tidal dissipation for an ice-covered
 489 moon.

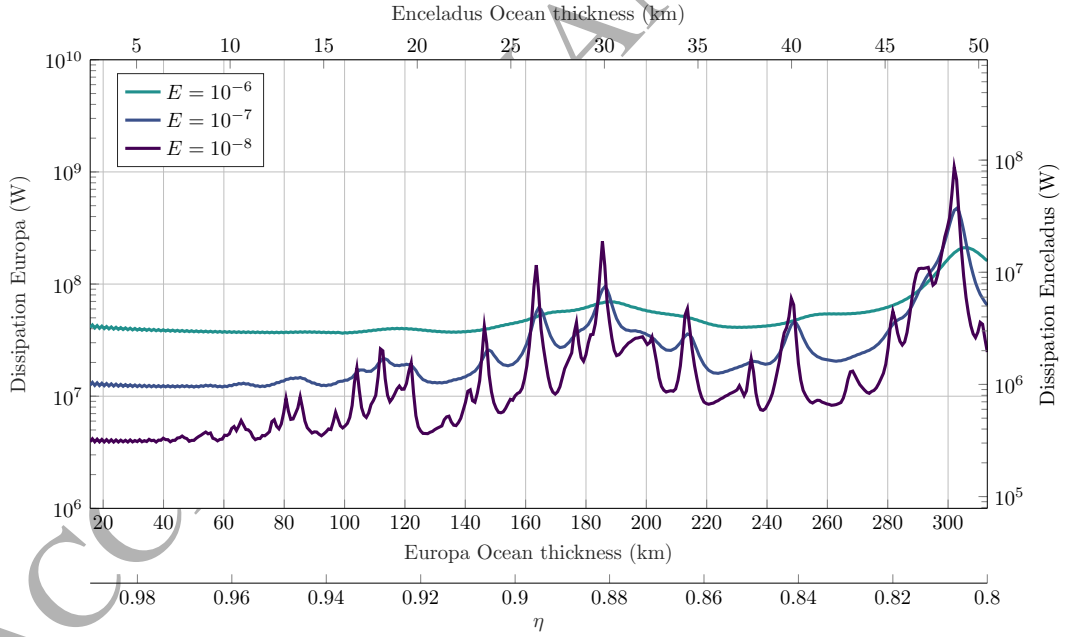
490 We find that dissipation depends strongly on ocean thickness and Ekman number. One
 491 of the challenges in computing tidal dissipation is the scarcity of information about Europa
 492 and Enceladus oceans. For instance, the effective viscosity, which depends on small-scale
 493 dissipative processes, is not known. It is for this reason that we analyse the behaviour of
 494 the fluid for a wide range of Ekman numbers. For a given ocean thickness we distinguish
 495 three different scenarios depending on the behaviour of dissipation with Ekman number. If
 496 a wave attractor is excited, an asymptotic limit is reached where dissipation is independent
 497 of viscosity. Otherwise, there can be an anti-resonance or resonance depending on the ocean
 498 geometry. Anti-resonant states, where we observe a decrease of dissipation with decreasing
 499 Ekman number, are attained for unrealistically thick oceans; while resonant states, where
 500 dissipation increases with decreasing Ekman number, are common for shallower oceans.

501 After analysing the effect of changing the ocean thickness and viscosity we conclude
 502 that under the aforementioned assumptions, tidal dissipation due to inertial waves is several
 503 orders of magnitude smaller than Europa's radiogenic heating and Enceladus' observed heat
 504 flux and thus does not play an important role in preventing these oceans from freezing.
 505 Still, we observe that the induced tidal currents can be one order of magnitude stronger
 506 than those obtained using the Laplace Tidal Equations (e.g., Tyler, 2008, 2009). We find
 507 that for a 30 km thick Enceladan ocean tidal currents of amplitude 3 cm/s are excited.
 508 We also consider the possible interaction of inertial waves and the ice shell and conclude
 509 that for global oceans of constant thickness it is unlikely that inertial waves could result in
 510 observable surface features.

511 The difficulty in explaining Enceladus' present state through tidal dissipation in its solid
 512 parts (ice and mantle) have led to a focus on tidal dissipation within the ocean in the past



(a)



(b)

Figure 6: (a) Tidal dissipation amplitude in an ocean contained within a spherical shell due to inertial waves excited by the degree-two order-zero eccentricity tide. The forcing frequency equals the rotational frequency of the body. Dissipation is given for varying ocean thickness, varying values of inner to outer ocean radius ratios (η) and Ekman number ranging from 10^{-4} to 10^{-8} . (b) is a zoom-in of (a) for the most relevant range of ocean thicknesses for Europa and Enceladus ($\eta = 0.8 - 1$).

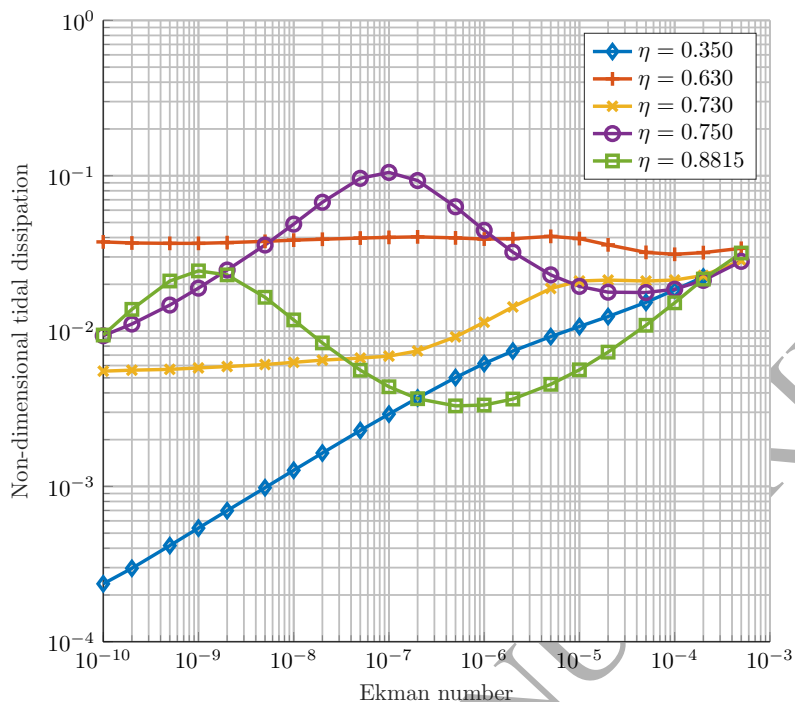


Figure 7: Non-dimensional tidal dissipation amplitude, as defined in Equation (B.4), as a function of Ekman number for different representative inner to outer ocean radius ratio (η) for the degree-two order-zero eccentricity tidal component. $\eta = 0.63, 0.73$, corresponds to an ocean with wave attractors with high (in absolute value) Lyapunov exponent; for $\eta = 0.35$ there is an antiresonance; and $\eta = 0.75, 0.8815$ correspond to two resonant states. The markers indicate the different numerical experiments performed.

513 years. However, so far tidal dissipation estimations using the Laplace Tidal Equations have
 514 resulted in low values of tidal dissipation for Enceladus' estimated ocean thickness (Tyler,
 515 2014; Hay and Matsuyama, 2017; Matsuyama et al., 2018). It was suggested that internal
 516 inertial waves might produce enough additional tidal dissipation. Here we show that the
 517 direct generation of inertial waves in a spherical shell does not provide significant additional
 518 heat to prevent the ocean from freezing either.

519 However, the discussion on tidal heating in the subsurface oceans of the icy moons is far
 520 from settled. In our study we have made several assumptions that need to be revisited. We
 521 have assumed the ocean to be (1) unstratified, (2) of constant-thickness (no topography),
 522 and (3) we have neglected non-linear effects. Each of these elements are discussed in the
 523 next paragraphs.

524 We are limited by the absence of direct observations of the extraterrestrial oceans. We
 525 do not have any information about their density structure, thus, we can only apply our
 526 knowledge of similar environments on Earth to make an educated guess. Following the
 527 suggestions of Goodman et al. (2004); Goodman and Lenferink (2012) we have considered
 528 the ocean to be convectively mixed. However, under some circumstances the ocean can
 529 be stratified (Melosh et al., 2004; Vance and Brown, 2005). In a stratified ocean, internal
 530 gravity waves, which play an important role in tidal dissipation on Earth (Garrett, 2003),

531 can also be generated, adding a new possible source of tidal dissipation.

532 In this study we consider an ocean contained within a spherical shell. However, it is
 533 expected that Enceladus' and Europa's ocean basins deviate from this idealised shape. It
 534 is known, for example, that Enceladus' ocean does not have a constant thickness. On the
 535 contrary, the ice shell thickness varies from 7 km at the south pole to 24 km at the equator
 536 (Beuthe et al., 2016; Čadek et al., 2016). Moreover, due to rotation and tidal deformations
 537 both Europa and Enceladus have the shape of a triaxial ellipsoid (e.g., Nimmo et al., 2007;
 538 Thomas, 2010). Wave attractors also exist in more general ocean basins. We expect that the
 539 conversion of large-scale tides into small scale inertial waves will be facilitated by additional
 540 topographic variations. Inertial waves for complex ocean geometries is an exciting topic for
 541 future work.

542 Besides, the barotropic tide given by the LTE highly depends on the ocean's basin
 543 geometry. The interaction of the barotropic horizontal currents with topography excites
 544 internal waves. On Earth most tidal dissipation occurs on the shallow continental shelf where
 545 barotropic currents have a higher amplitude, but an additional $\sim 30\%$ of tidal dissipation
 546 occurs in the oceanic ridges due to the excitation of internal waves (Egbert and Ray, 2000,
 547 2003). The effect of topography on both the barotropic and internal tide should be further
 548 studied.

549 Finally, in this study we have used perturbation theory, we have ignored the non-linear
 550 terms in the momentum equations. The use of non-linear terms would change the behaviour
 551 of the fluid. For example, inertial waves could interact with the underlying convective flow.
 552 Another possible interaction is that of inertial waves with a mean-flow excited by libration
 553 which can lead to the well-known elliptic instability (Kerswell, 2002). This flow instabil-
 554 ity gives rise to fully three dimensional turbulence which might enhance dissipation and
 555 change its geographical pattern. Both Europa and Enceladus might be subject to this in-
 556 stability (Lemasquerier et al., 2017). Further experimental and numerical work is needed to
 557 understand the relevance of this phenomenon in heating the icy moons and shaping their
 558 surface.

559 **Acknowledgement**

560 This research has been financially supported by the Space Research User Support pro-
 561 gram of the Netherlands Organization for Scientific Research (NWO) under contract number
 562 ALW-GO/16-19. The authors would like to thank the editor F. Nimmo and two anony-
 563 mous reviewers for their valuable comments and suggestions which helped to improve the
 564 manuscript.

565 **Appendix A. Numerical approach expanded**

566 We solve Equations (19) using the spectral method of Rieutord and Valdettaro (1997).
 567 We expand the different fields using vector spherical harmonics:

$$\mathbf{u}^{(d)} = \sum_{l=0}^{\infty} \sum_{m=-l}^l [u_m^l(r)\mathbf{R}_l^m + v_m^l(r)\mathbf{S}_l^m + w_m^l(r)\mathbf{T}_l^m] \quad (\text{A.1a})$$

$$W = \sum_{l=0}^{\infty} \sum_{m=-l}^l W_m^l(r)Y_l^m(\theta, \phi) \quad (\text{A.1b})$$

with:

$$\mathbf{R}_l^m = Y_l^m \mathbf{e}_r \quad \mathbf{S}_l^m = \nabla Y_l^m \quad \mathbf{T}_l^m = \nabla \times \mathbf{R}_l^m \quad (\text{A.2})$$

where Y_l^m are normalized spherical harmonics which satisfy the following orthogonal relations:

$$\int_{4\pi} \mathbf{R}_l^m \cdot \mathbf{S}_l^{m'} d\Omega = \int_{4\pi} \mathbf{S}_l^m \cdot \mathbf{T}_l^{m'} d\Omega = \int_{4\pi} \mathbf{T}_l^m \cdot \mathbf{R}_l^{m'} d\Omega = 0 \quad (\text{A.3a})$$

$$\int_{4\pi} \mathbf{R}_l^m \cdot \mathbf{R}_l^{m'} d\Omega = \delta_{ll'} \delta_{mm'} \quad (\text{A.3b})$$

$$\int_{4\pi} \mathbf{S}_l^m \cdot \mathbf{S}_l^{m'} d\Omega = \int_{4\pi} \mathbf{T}_l^m \cdot \mathbf{T}_l^{m'} d\Omega = l(l+1) \delta_{ll'} \delta_{mm'}. \quad (\text{A.3c})$$

Using the previous expansion the continuity equation becomes:

$$v_m^l = \frac{1}{l(l+1)r} \frac{\partial r^2 u_m^l}{\partial r}. \quad (\text{A.4})$$

Taking the curl of Equation (15) to eliminate the potential and introducing Equation (A.4) we get the following Equations for the \mathbf{R}_l^m , and \mathbf{T}_l^m velocity components:

$$E \Delta_l w_m^l + \left(\frac{im}{l(l+1)} - i\omega \right) w_m^l = -A(l, m) r^{l-1} \frac{d}{dr} \left(\frac{u_m^{l-1}}{r^{l-2}} \right) - A(l+1, m) r^{-l-2} \frac{d}{dr} (r^{l+3} u_m^{l+1}) + f_R, \quad (\text{A.5a})$$

$$E \Delta_l \Delta_l (r u_m^l) + \left(\frac{im}{l(l+1)} - i\omega \right) \Delta_l (r u_m^l) = B(l, m) r^{l-1} \frac{d}{dr} \left(\frac{w_m^{l-1}}{r^{l-1}} \right) + B(l+1, m) r^{-l-2} \frac{d}{dr} (r^{l+2} w_m^{l+1}) + f_T; \quad (\text{A.5b})$$

with:

$$A(l, m) = \frac{1}{l^2} \sqrt{\frac{l^2 - m^2}{4l^2 - 1}}, \quad B(l, m) = l^2(l^2 - 1)A(l, m); \quad \Delta_l = \frac{1}{r} \frac{d^2}{dr^2} r - \frac{l(l+1)}{r^2}. \quad (\text{A.6})$$

580 The forcing terms f_R and f_T are given by :

$$f_R = -\frac{r}{l(l+1)} \nabla \times \mathbf{f}^{(eq)} \cdot \mathbf{R}_l^m \quad (\text{A.7a})$$

$$f_T = l(l+1) \nabla \times \mathbf{f}^{(eq)} \cdot \mathbf{T}_l^m \quad (\text{A.7b})$$

581 The values of f_T and f_R are obtained for the different tidal constituents. We need
582 to obtain the non-dimensional components of the different constituents of the equilibrium
583 tide \mathbf{u}_{eq} in terms of spherical harmonics. We compute their amplitude by taking the time
584 derivative of Equation (6) and using the definition of the equilibrium tide given in Equation
585 (16). We write the resulting expressions using the previously defined normalised spherical
586 harmonics $Y_{l,m}$:

$$\mathbf{u}_{e0}^{(eq)} = -i \frac{3}{2} \sqrt{\frac{\pi}{5}} \frac{\omega^2 e R}{g} r^2 \mathbf{R}_2^0 = k_{e0} i r^2 \mathbf{R}_2^0 \quad (\text{A.8a})$$

$$\mathbf{u}_{o1e}^{(eq)} = -\sqrt{\frac{3\pi}{5}} \frac{\omega^2 R \sin \epsilon}{2g} r^2 \mathbf{R}_2^1 = -k_{o1e} r^2 \mathbf{R}_2^1 \quad (\text{A.8b})$$

$$\mathbf{u}_{o1w}^{(eq)} = \sqrt{\frac{3\pi}{5}} \frac{\omega^2 R \sin \epsilon}{2g} r^2 \mathbf{R}_2^1 = k_{o1w} r^2 \mathbf{R}_2^1 \quad (\text{A.8c})$$

$$\mathbf{u}_{e2e}^{(eq)} = i \frac{7}{4} \sqrt{\frac{6\pi}{5}} \frac{\omega^2 e R}{g} r^2 \mathbf{R}_2^2 = k_{e2e} i r^2 \mathbf{R}_2^2 \quad (\text{A.8d})$$

$$\mathbf{u}_{e2w}^{(eq)} = -i \frac{1}{4} \sqrt{\frac{6\pi}{5}} \frac{\omega^2 e R}{g} r^2 \mathbf{R}_2^2 = k_{e2w} i r^2 \mathbf{R}_2^2. \quad (\text{A.8e})$$

587 Introducing Equation (A.8) into Equation (A.7) we can get the values of f_R and f_T for
588 $m = 0$, $m = 1$ and $m = 2$ components, ($f_R^0, f_T^0, f_R^1, f_T^1$ and f_R^2, f_T^2).

$$f_R^0 = k_{e0} i \frac{r^2}{\sqrt{35}} \delta_{l,3} - k_{e0} i \frac{r^2}{\sqrt{15}} \delta_{l,1}, \quad f_T^0 = 6k_{e0} \omega r \delta_{l,2} \quad (\text{A.9a})$$

$$f_R^1 = k_{o1} \frac{2r^2}{3} \sqrt{\frac{2}{35}} \delta_{l,3} - k_{o1} \frac{r^2}{2} \sqrt{\frac{3}{15}} \delta_{l,1}, \quad f_T^1 = -6k_{o1} i r (\omega + \frac{1}{2}) \delta_{l,2} \quad (\text{A.9b})$$

$$f_R^2 = k_{e2} i \frac{r^2}{\sqrt{63}} \delta_{l,3}, \quad f_T^2 = 6k_{e2} \omega r \delta_{2,l} + 6k_{e2} r \delta_{l,2}. \quad (\text{A.9c})$$

591 k_{e2e} (k_{o1e}) or k_{e2w} (k_{o1w}) should be used in the place of k_{e2} (k_{o1}) depending if we solve for
592 the westward or eastward wave. Note that the constant k contains information about the
593 physical characteristics of each moon. Due to the fact that the PDEs are linear we solve the
594 system for $k = 1$ and multiply the solution by the corresponding value of k to obtain the
595 solution for each configuration.

By inspecting Equations A.5 it is clear that the different orders are decoupled, but there exists a coupling between degrees. However, not all the degrees are coupled, symmetric (\mathbf{X}_m^+) and antisymmetric (\mathbf{X}_m^-) modes with respect to the equator are decoupled and can be solved independently.

$$\mathbf{X}_m^+ = \begin{bmatrix} u_m^m \\ w_m^{m+1} \\ u_m^{m+2} \\ w_m^{m+3} \\ \vdots \end{bmatrix} \quad \mathbf{X}_m^- = \begin{bmatrix} w_m^m \\ u_m^{m+1} \\ w_m^{m+2} \\ u_m^{m+3} \\ \vdots \end{bmatrix}. \quad (\text{A.10})$$

Note that for the $m = 0$ and $m = 2$ tidal components the \mathbf{X}_0^+ and the \mathbf{X}_2^+ solutions are excited, respectively, while $m = 1$ excites the \mathbf{X}_1^- solution.

The partial differential equations A.5 are discretised in the radial direction using the Chebyshev polynomials on the Gauss-Lobatto collocation nodes (see Section 3.3). More details about this method can be found in Rieutord and Valdettaro (1997).

Appendix B. Tidal dissipation computation

We expand Equation (20) as:

$$\hat{D}_v = E \int_{\eta}^1 d(r) r^2 dr, \quad (\text{B.1})$$

where $d(r)$ is the dissipation in a spherical layer with radius r . We can write the previous equation using the spherical harmonic decomposition of the velocity (Equation (A.1)):

$$d(r) = \sum_{l=0}^L \sum_{m=-L}^L 3 \left| \frac{\partial u_m^l}{\partial r} \right|^2 + l(l+1)(|s_m^l|^2 + |t_m^l|^2) + (l-1)l(l+1)(l+2) \frac{|v_m^l|^2 + |w_m^l|^2}{r^2}, \quad (\text{B.2})$$

with:

$$s_m^l = \frac{\partial v_m^l}{\partial r} + \frac{u_m^l - v_m^l}{r} \quad (\text{B.3a})$$

$$t_m^l = r \frac{\partial w_m^l}{\partial r} \frac{1}{r}. \quad (\text{B.3b})$$

e.g. Rieutord (1987). The total value of \hat{D}_v is obtained by numerically integrating Equation (B.1). Finally, we obtain the dimensional value as:

$$D_v = 8k^2 \rho_o \omega^3 R^5 \hat{D}_v \quad (\text{B.4})$$

where k depends on the tidal component considered and is given by Equation (A.8).

614 **References**

- 615 Anderson, J. D., Schubert, G., Jacobson, R. A., Lau, E. L., Moore, W. B., Sjogren, W. L., 1998. Europa's
 616 differentiated internal structure: Inferences from four galileo encounters. *Science* 281 (5385), 2019–2022.
 617 URL <https://doi.org/10.1126/science.281.5385.2019>
- 618 Baland, R.-M., Yseboodt, M., Van Hoolst, T., 2012. Obliquity of the Galilean satellites: The influence of a
 619 global internal liquid layer. *Icarus* 220 (2), 435 – 448.
 620 URL <https://doi.org/10.1016/j.icarus.2012.05.020>
- 621 Běhounková, M., Souček, O., Jaroslav, H., Čadek, O., 2017. Plume activity and tidal deformation on
 622 Enceladus influenced by faults and variable ice shell thickness. *Astrobiology* 17 (9), 941–954.
 623 URL <https://doi.org/10.1089/ast.2016.1629>
- 624 Beuthe, M., 2016. Crustal control of dissipative ocean tides in Enceladus and other icy moons. *Icarus* 280,
 625 278 – 299.
 626 URL <https://doi.org/10.1016/j.icarus.2016.08.009>
- 627 Beuthe, M., Rivoldini, A., Trinh, A., 2016. Enceladus's and Dione's floating ice shells supported by minimum
 628 stress isostasy. *Geophys. Res. Lett.* 43 (19), 10,088–10,096.
 629 URL <http://dx.doi.org/10.1002/2016GL070650>
- 630 Bretherton, F. P., 1964. Low frequency oscillations trapped near the equator. *Tellus* 16 (2), 181–185.
 631 URL <http://dx.doi.org/10.1111/j.2153-3490.1964.tb00159.x>
- 632 Brouzet, C., Ermanyuk, E. V., Joubaud, S., Sibgatullin, I., Dauxois, T., 2016. Energy cascade in internal-
 633 wave attractors. *Europhys. Lett.* 113 (4), 44001.
 634 URL <https://doi.org/10.1209/0295-5075/113/44001>
- 635 Bryan, G., 1889. The waves on a rotating liquid spheroid of finite ellipticity. *Phil. Trans. R. Soc. A* 180,
 636 187–219.
 637 URL <http://doi.org/10.1098/rsta.1889.0006>
- 638 Čadek, O., Tobie, G., Van Hoolst, T., Mass, M., Choblet, G., Lefèvre, A., Mitri, G., Baland, R.-M.,
 639 Běhounková, M., Bourgeois, O., Trinh, A., 2016. Enceladus's internal ocean and ice shell constrained
 640 from Cassini gravity, shape, and libration data. *Geophys. Res. Lett.* 43 (11), 5653–5660.
 641 URL <http://dx.doi.org/10.1002/2016GL068634>
- 642 Cassen, P., Reynolds, R. T., Peale, S. J., 1979. Is there liquid water on Europa? *Geophys. Res. Lett.* 6 (9),
 643 731–734.
 644 URL <http://dx.doi.org/10.1029/GL006i009p00731>
- 645 Chen, E., Nimmo, F., Glatzmaier, G., 2014. Tidal heating in icy satellite oceans. *Icarus* 229, 11 – 30.
 646 URL <https://doi.org/10.1016/j.icarus.2013.10.024>
- 647 Chen, E. M. A., Nimmo, F., 2011. Obliquity tides do not significantly heat Enceladus. *Icarus* 214 (2), 779–
 648 781.
 649 URL <https://doi.org/10.1016/j.icarus.2011.06.0078>
- 650 Choblet, G., Tobie, G., Sotin, C., Běhounková, M., Čadek, O., Postberg, F., Souček, O., 2017. Powering
 651 prolonged hydrothermal activity inside Enceladus. *Nat. Astron.* 1 (12), 841–847.
 652 URL <https://doi.org/10.1038/s41550-017-0289-8>
- 653 Egbert, G. D., Ray, R. D., 2000. Significant dissipation of tidal energy in the deep ocean inferred from
 654 satellite altimeter data. *Nature* 405, 775.
 655 URL <http://dx.doi.org/10.1038/35015531> <http://10.0.4.14/35015531>
- 656 Egbert, G. D., Ray, R. D., 2003. Semidiurnal and diurnal tidal dissipation from TOPEX/Poseidon altimetry.
 657 *Geophys. Res. Lett.* 30 (17).
 658 URL <https://doi.org/10.1029/2003GL017676>
- 659 Garrett, C., 2003. Internal tides and ocean mixing. *Science* 301 (5641), 1858–1859.
 660 URL <http://doi.org/10.1126/science.1090002>
- 661 Gerkema, T., Zimmerman, J. T. F., Maas, L. R. M., van Haren, H., 2008. Geophysical and astrophysical
 662 fluid dynamics beyond the traditional approximation. *Rev. Geophys.* 46 (2), 1–33.
 663 URL <http://dx.doi.org/10.1029/2006RG000220>
- 664 Goodman, J. C., Collins, G. C., Marshall, J., Pierrehumbert, R. T., 2004. Hydrothermal plume dynamics

- 665 on Europa: Implications for chaos formation. *J. Geophys. Res. Planets* 109 (E3).
 666 URL <http://dx.doi.org/10.1029/2003JE002073>
- 667 Goodman, J. C., Lenferink, E., 2012. Numerical simulations of marine hydrothermal plumes for Europa and
 668 other icy worlds. *Icarus* 221 (2), 970 – 983.
 669 URL <https://doi.org/10.1016/j.icarus.2012.08.027>
- 670 Greenspan, H. P., 1969. *The Theory of Rotating Fluids*. Cambridge University press, Cambridge Mono-
 671 graphs on Mechanics and Applied Mathematics, New York.
- 672 Hay, H. C., Matsuyama, I., 2017. Numerically modelling tidal dissipation with bottom drag in the oceans
 673 of Titan and Enceladus. *Icarus* 281, 342 – 356.
 674 URL <https://doi.org/10.1016/j.icarus.2016.09.022>
- 675 Hollerbach, R., Kerswell, R. R., 1995. Oscillatory internal shear layers in rotating and precessing flows. *J.*
 676 *Fluid Mech.* 298, 327–339.
 677 URL <https://doi.org/10.1017/S0022112095003338>
- 678 Hsu, H.-W., Postberg, F., Sekine, Y., Shibuya, T., Kempf, S., Horányi, M., Juhász, A., Altobelli, N., Suzuki,
 679 K., Masaki, Y., Kuwatani, T., Tachibana, S., Sirono, S., Moragas-Klostermeyer, G., Srama, R., 2015.
 680 Ongoing hydrothermal activities within Enceladus. *Nature* 519, 207–210.
 681 URL <http://dx.doi.org/10.1038/nature14262>
- 682 Hussmann, H., Choblet, G., Lainey, V., Matson, D. L., Sotin, C., Tobie, G., Van Hoolst, T., 2010. Implica-
 683 tions of rotation, orbital states, energy sources, and heat transport for internal processes in icy satellites.
 684 *Space Sci. Rev.* 153 (1), 317–348.
 685 URL <https://doi.org/10.1007/s11214-010-9636-0>
- 686 Hussmann, H., Spohn, T., Wiczerkowski, K., 2002. Thermal equilibrium states of europa’s ice shell: Impli-
 687 cations for internal ocean thickness and surface heat flow. *Icarus* 156 (1), 143 – 151.
 688 URL <https://doi.org/10.1006/icar.2001.6776>
- 689 Jara-Orué, H. M., Vermeersen, B. L., 2011. Effects of low-viscous layers and a non-zero obliquity on surface
 690 stresses induced by diurnal tides and non-synchronous rotation: The case of Europa. *Icarus* 215 (1), 417
 691 – 438.
 692 URL <https://doi.org/10.1016/j.icarus.2011.05.034>
- 693 Kerswell, R. R., 1995. On the internal shear layers spawned by the critical regions in oscillatory ekman
 694 boundary layers. *J. Fluid Mech.* 298, 311–325.
 695 URL <http://doi.org/10.1017/S0022112095003326>
- 696 Kerswell, R. R., 2002. Elliptical instability. *Annu. Rev. Fluid Mech.* 34 (1), 83–113.
 697 URL <https://doi.org/10.1146/annurev.fluid.34.081701.171829>
- 698 Khurana, K. K., Kivelson, M. G., Stevenson, D. J., Schubert, G., Russell, C. T., Walker, R. J., Polanskey, C.,
 699 1998. Induced magnetic fields as evidence for subsurface oceans in Europa and Callisto. *Nature* 395 (6704),
 700 777–780.
 701 URL <http://dx.doi.org/10.1038/27394>
- 702 Kivelson, M. G., Khurana, K. K., Russell, C. T., Volwerk, M., Walker, R. J., Zimmer, C., 2000. Galileo
 703 magnetometer measurements: A stronger case for a subsurface ocean at Europa. *Science* 289 (5483),
 704 1340–1343.
 705 URL <http://doi.org/10.1126/science.289.5483.1340>
- 706 Lainey, V., Jacobson, R. A., Tajeddine, R., Cooper, N. J., Murray, C., Robert, V., Tobie, G., Guillot, T.,
 707 Mathis, S., Remus, F., Desmars, J., Arlot, J.-E., Cuyper, J.-P. D., Dehant, V., Pascu, D., Thuillot, W.,
 708 Poncin-Lafitte, C. L., Zahn, J.-P., 2017. New constraints on Saturn’s interior from Cassini astrometric
 709 data. *Icarus* 281, 286 – 296.
 710 URL <https://doi.org/10.1016/j.icarus.2016.07.014>
- 711 Le Bars, M., Cbron, D., Le Gal, P., 2015. Flows driven by libration, precession, and tides. *Annual Review*
 712 *of Fluid Mechanics* 47 (1), 163–193.
 713 URL <https://doi.org/10.1146/annurev-fluid-010814-014556>
- 714 Lemasquerier, D., Grannan, A. M., Vidal, J., D., C., Favier, B., Le Bars, M., Aurnou, J. M., 2017. Libra-
 715 tion-driven flows in ellipsoidal shells. *J. Geophys. Res. Planets* 122 (9), 1926–1950.

- 716 URL <https://doi.org/10.1002/2017JE005340>
- 717 Longuet-Higgins, M. S., 1968. The eigenfunctions of Laplace's tidal equations over a sphere. *Phil. Trans. R.*
718 *Soc. A* 262 (1132), 511–607.
- 719 URL <http://doi.org/10.1098/rsta.1968.0003>
- 720 Maas, L. R. M., 2001. Wave focusing and ensuing mean flow due to symmetry breaking in rotating fluids.
721 *J. Fluid Mech.* 437, 13–28.
- 722 URL <http://doi.org/10.1017/S0022112001004074>
- 723 Maas, L. R. M., 2005. Wave attractors: Linear yet nonlinear. *Int. J. Bifurcat. Chaos* 15 (09), 2757–2782.
- 724 URL <http://doi.org/10.1142/S0218127405013733>
- 725 Maas, L. R. M., Benielli, D., Sommeria, J., Lam, F.-P. A., Aug. 1997. Observation of an internal wave
726 attractor in a confined, stably stratified fluid. *Nature* 388 (6642), 557–561.
- 727 URL <https://doi.org/10.1038/41509>
- 728 Manders, A. M. M., Maas, L. R. M., 2003. Observations of inertial waves in a rectangular basin with one
729 sloping boundary. *J. Fluid Mech.* 493, 59–88.
- 730 URL <http://doi.org/10.1017/S0022112003005998>
- 731 Manders, A. M. M., Maas, L. R. M., 2004. On the three-dimensional structure of the inertial wave field in
732 a rectangular basin with one sloping boundary. *Fluid Dyn. Res.* 35 (1), 1–21.
- 733 URL <https://doi.org/10.1016/j.fluiddyn.2004.03.004>
- 734 Matsuyama, I., Beuthe, M., Hay, H. C., Nimmo, F., Kamata, S., 2018. Ocean tidal heating in icy satellites
735 with solid shells. *Icarus* 312, 208 – 230.
- 736 URL <https://doi.org/10.1016/j.icarus.2018.04.013>
- 737 Melosh, H., Ekholm, A., Showman, A., Lorenz, R., 2004. The temperature of Europa's subsurface water
738 ocean. *Icarus* 168 (2), 498 – 502.
- 739 URL <https://doi.org/10.1016/j.icarus.2003.11.021>
- 740 Nimmo, F., Thomas, P., Pappalardo, R., Moore, W., 2007. The global shape of Europa: Constraints on
741 lateral shell thickness variations. *Icarus* 191 (1), 183 – 192.
- 742 URL <https://doi.org/10.1016/j.icarus.2007.04.021>
- 743 Ogilvie, G. I., 2005. Wave attractors and the asymptotic dissipation rate of tidal disturbances. *J. Fluid*
744 *Mech.* 543, 19–44.
- 745 URL <http://doi.org/10.1017/S0022112005006580>
- 746 Ogilvie, G. I., 2009. Tidal dissipation in rotating fluid bodies: a simplified model. *Mon. Not. R. Astron. Soc.*
747 396 (2), 794–806.
- 748 URL <http://dx.doi.org/10.1111/j.1365-2966.2009.14814.x>
- 749 Ogilvie, G. I., Lin, D. N. C., 2004. Tidal dissipation in rotating giant planets. *Astrophys. J.* 610 (1), 477–509.
- 750 URL <http://doi.org/10.1086/421454>
- 751 Ojakangas, G. W., Stevenson, D. J., 1989. Thermal state of an ice shell on Europa. *Icarus* 81 (2), 220 – 241.
- 752 URL [https://doi.org/10.1016/0019-1035\(89\)90052-3](https://doi.org/10.1016/0019-1035(89)90052-3)
- 753 Pappalardo, R. T., Belton, M. J. S., Breneman, H. H., Carr, M. H., Chapman, C. R., Collins, G. C., Denk,
754 T., Fagents, S., Geissler, P. E., Giese, B., Greeley, R., Greenberg, R., Head, J. W., Helfenstein, P., Hoppa,
755 G., Kadel, S. D., Klaasen, K. P., Klemaszewski, J. E., Magee, K., McEwen, A. S., Moore, J. M., Moore,
756 W. B., Neukum, G., Phillips, C. B., Prockter, L. M., Schubert, G., Senske, D. A., Sullivan, R. J., Tufts,
757 B. R., Turtle, E. P., Wagner, R., Williams, K. K., 1999. Does Europa have a subsurface ocean? Evaluation
758 of the geological evidence. *J. Geophys. Res. Planets* 104 (E10), 24015–24055.
- 759 URL <http://dx.doi.org/10.1029/1998JE000628>
- 760 Porco, C. C., Helfenstein, P., Thomas, P. C., Ingersoll, A. P., Wisdom, J., West, R., Neukum, G., Denk, T.,
761 Wagner, R., Roatsch, T., Kieffer, S., Turtle, E., McEwen, A., Johnson, T. V., Rathbun, J., Veverka, J.,
762 Wilson, D., Perry, J., Spitale, J., Brahic, A., Burns, J. A., DelGenio, A. D., Dones, L., Murray, C. D.,
763 Squyres, S., 2006. Cassini observes the active South Pole of Enceladus. *Science* 311 (5766), 1393–1401.
- 764 URL <http://doi.org/10.1126/science.1123013>
- 765 Postberg, F., Kempf, S., Schmidt, J., Brilliantov, N., Beinsen, A., Abel, B., Buck, U., Srama, R., 2009.
766 Sodium salts in E-ring ice grains from an ocean below the surface of Enceladus. *Nature* 459, 1098–1101.

- 767 URL <http://dx.doi.org/10.1038/nature08046>
- 768 Postberg, F., Schmidt, J., Hillier, J., Kempf, S., Srama, R., 2011. A salt-water reservoir as the source of a
769 compositionally stratified plume on Enceladus. *Nature* 474, 620–622.
- 770 URL <http://dx.doi.org/10.1038/nature10175>
- 771 Rabitti, A., Maas, L. R., 2014. Inertial wave rays in rotating spherical fluid domains. *J. Fluid Mech.* 758,
772 621–654.
- 773 URL <https://doi.org/10.1017/jfm.2014.551>
- 774 Rabitti, A., Maas, L. R. M., 2013. Meridional trapping and zonal propagation of inertial waves in a rotating
775 fluid shell. *J. Fluid Mech.* 729, 445–470.
- 776 URL <https://doi.org/10.1017/jfm.2013.310>
- 777 Rieutord, M., 1987. Linear theory of rotating fluids using spherical harmonics part I: Steady flows. *Geophys.*
778 *Astro. Fluid* 39 (3), 163–182.
- 779 URL <http://dx.doi.org/10.1080/03091928708208811>
- 780 Rieutord, M., Georgeot, B., Valdetaro, L., 2001. Inertial waves in a rotating spherical shell: attractors and
781 asymptotic spectrum. *J. Fluid Mech.* 435, 103–144.
- 782 URL <http://doi.org/10.1017/S0022112001003718>
- 783 Rieutord, M., Valdetaro, L., 1997. Inertial waves in a rotating spherical shell. *J. Fluid Mech.* 341, 77–99.
- 784 URL <http://doi.org/10.1017/S0022112097005491>
- 785 Rieutord, M., Valdetaro, L., 2010. Viscous dissipation by tidally forced inertial modes in a rotating spherical
786 shell. *J. Fluid Mech.* 643, 363–394.
- 787 URL <http://doi.org/10.1017/S002211200999214X>
- 788 Rieutord, M., Valdetaro, L., Jun. 2018. Axisymmetric inertial modes in a spherical shell at low Ekman
789 numbers. *J. Fluid Mech.* 844, 597–634.
- 790 URL <http://doi.org/10.1017/jfm.2018.201>
- 791 Roberts, J. H., Nimmo, F., 2008. Tidal heating and the long-term stability of a subsurface ocean on Ence-
792 ladus. *Icarus* 194 (2), 675 – 689.
- 793 URL <https://doi.org/10.1016/j.icarus.2007.11.010>
- 794 Soderlund, K. M., Schmidt, B. E., Wicht, J., Blankenship, D. D., 2013. Ocean-driven heating of Europa's
795 icy shell at low latitudes. *Nat. Geosci.* 7, 16–19.
- 796 URL <http://dx.doi.org/10.1038/ngeo2021>
- 797 Spencer, J. R., Howett, C. J. A., Verbiscer, A., Hurford, T. A., Segura, M., Spencer, D. C., Sep. 2013.
798 Enceladus heat flow from high spatial resolution thermal emission observations. *European Planetary*
799 *Science Congress Abstracts* 8.
- 800 Spencer, J. R., Pearl, J. C., Segura, M., Flasar, F. M., Mamoutkine, A., Romani, P., Buratti, B. J., Hendrix,
801 A. R., Spilker, L. J., Lopes, R. M. C., 2006. Cassini encounters Enceladus: Background and the discovery
802 of a south polar hot spot. *Science* 311 (5766), 1401–1405.
- 803 URL <http://doi.org/10.1126/science.1121661>
- 804 Stern, M. E., 1963. Trapping of low frequency oscillations in an equatorial boundary layer. *Tellus* 15 (3),
805 246–250.
- 806 URL <http://dx.doi.org/10.1111/j.2153-3490.1963.tb01384.x>
- 807 Stewartson, K., 1971. On trapped oscillations of a rotating fluid in a thin spherical shell. *Tellus* 23 (6),
808 506–510.
- 809 URL <http://dx.doi.org/10.1111/j.2153-3490.1971.tb00598.x>
- 810 Stewartson, K., 1972. On trapped oscillations of a rotating fluid in a thin spherical shell ii. *Tellus* 24 (4),
811 283–287.
- 812 URL <http://dx.doi.org/10.1111/j.2153-3490.1972.tb01555.x>
- 813 Thomas, P., 2010. Sizes, shapes, and derived properties of the saturnian satellites after the cassini nominal
814 mission. *Icarus* 208 (1), 395 – 401.
- 815 URL <https://doi.org/10.1016/j.icarus.2010.01.025>
- 816 Thomas, P., Tajeddine, R., Tiscareno, M., Burns, J., Joseph, J., Loredo, T., Helfenstein, P., Porco, C., 2016.
817 Enceladus's measured physical libration requires a global subsurface ocean. *Icarus* 264, 37 – 47.

- 818 URL <https://doi.org/10.1016/j.icarus.2015.08.037>
- 819 Tobie, G., Čadež, O., Sotin, C., 2008. Solid tidal friction above a liquid water reservoir as the origin of the
820 south pole hotspot on Enceladus. *Icarus* 196 (2), 642–652.
- 821 URL <https://doi.org/10.1016/j.icarus.2008.03.008>
- 822 Tyler, R. H., 2008. Strong ocean tidal flow and heating on moons of the outer planets. *Nature* 456 (7223),
823 770–772.
- 824 URL <http://dx.doi.org/10.1038/nature07571>
- 825 Tyler, R. H., 2009. Ocean tides heat Enceladus. *Geophys. Res. Lett.* 36 (15), L15205.
- 826 URL <http://dx.doi.org/10.1029/2009GL038300>
- 827 Tyler, R. H., 2014. Comparative estimates of the heat generated by ocean tides on icy satellites in the outer
828 solar system. *Icarus* 243 (Supplement C), 358–385.
- 829 URL <https://doi.org/10.1016/j.icarus.2014.08.037>
- 830 Vallis, G. K., 2006. *Atmospheric and Oceanic Fluid Dynamics*. Cambridge University Press, Cambridge,
831 U.K.
- 832 Vance, S., Brown, J., 2005. Layering and double-diffusion style convection in Europa's ocean. *Icarus* 177 (2),
833 506–514.
- 834 URL <https://doi.org/10.1016/j.icarus.2005.06.005>
- 835 Vermeersen, B. L., Maas, L. R., van Oers, S., Rabitti, A., Jara-Orue, H., 2013. Tidal-Induced Ocean
836 Dynamics as Cause of Enceladus' Tiger Stripe Pattern. AGU Fall Meeting Abstracts, P53B–1848.